Using Radar and Seismic Methods for the Determination of Ice Column Properties and Basal Conditions at Jakobshavn Isbræ and the NEEM Drill Site

By:

José A. Vélez González
M.S, University of Kansas

Submitted to the Department of Geology and Faculty of the Graduate School of The University of Kansas in partial fulfillment of the requirements for the degree of PhD of Science 2015

_____

Dr. George Tsoflias, Chair

_____

Dr. Ross Black, Committee Member

_____

Dr. JiLu Li, Committee Member

_____

Dr. Leigh A. Stearns, Committee Member

_____

Dr. Cornelis J. van der Veen, Committee Member

Date Defended: April 8, 2015

The dissertation Committee for José A. Vélez González certifies
That this is the approved version of the following dissertation:

Using Radar and Seismic Methods for the Determination of Ice Column Properties and Basal Conditions at Jakobshavn Isbræ and the NEEM Drill Site

_____

Dr. George Tsoflias, Chair

Date Approved: May 6, 2015

ABSTRACT

The development of preferred crystal orientation fabrics (COF) within the ice column can have a strong influence on the flow behavior of an ice sheet or glacier. Typically, COF information comes from ice cores. Observations of anisotropic seismic wave propagation and backscatter variation as a function of antenna orientation in GPR measurements have been proposed as methods to detect COF. For this investigation I evaluate the effectiveness of the GPR and seismic methods to detect COF by conducting a seismic and GPR experiment at the North Greenland Eemian Ice Drilling facility (NEEM) ice core location, where COF data is available.

The seismic experiment was conducted 6.5 km North West of the NEEM facility and consisted of three multi-offset seismic gathers. The results of the anisotropy analysis conducted at NEEM yielded mean c-axes distributed over a conical region of I angle of 30 to 32 degrees. No internal ice reflectors were imaged. Direct COF measurements collected in the ice core are in agreement with the results from the seismic anisotropy analysis.

The GPR experiment covered an area of 100 km^2 and consisted of parallel, perpendicular, oblique and circular (radius: 35 m) acquisition patterns. Results show evidence for COF for the entire 100 km^2 area. Furthermore, for the first time it was possible to image three different COF (random, disk and single maxima) and their respective transition zones. The interpretation of the GPR experiment showed a strong correlation with the ice core measurements.

Glacier basal drag is also an important, and difficult to predict, property that influences glacier flow. For this investigation I re-processed a 10 km-long high-resolution reflection seismic line at Jakobshavn Isbræ, Greenland, using an iterative velocity determination approach for

optimizing sub-glacier imaging. The resultant line imaged a sub-glacier sediment layer ranging in thickness between 35 and 200 meters. I interpret three distinct seismic facies based on the geometry of the reflectors as a basal till layer, accreted sediments and re-worked till. The basal till and accreted sediments vary in thickness between 4 and 93 meters and are thought to be water-saturated actively-deforming sub-glacier sediments. A polarity reversal observed at one location along the ice-sediment interface suggests the presence of water saturated sediments or water ponding 2-4 m thick spanning approximately 240 m across.

Using information from the seismic line (bed geometry, ice thickness, till thickness) as well as information available for the area of study (ice surface elevation and ice flow velocity) we evaluate the effect of sub-glacier sediment viscosity on the basal drag using a linearly viscous model and the assumption of a deforming bed. Basal drag values estimated for the study area fall within the range of physically acceptable values. However, the analysis revealed that the assumption of a deforming bed might not be compatible for the area of study given the presence of water at the ice/bed interface.

ACKNOWLEDGMENTS

This work was made possible by the Harry Jenkins Pre-Doctoral NASA fellowship, the National Science Foundation and the Center for Remote Sensing of Ice Sheets (CReSIS) (Grant No. ANT-0424589) in collaboration with Penn State Ice and Climate Exploration (Sridhar Anandakrishnan, Leo Peters, Kiya Riverman, Atsuhiro Muto, Knut Christianson and Don Voigt). I would like to express appreciation to J.P. Steffensen, Dorthe Dahl-Jensen and all the staff members at NEEM for their support in this investigation. In particular, I would like to thank my advisors (Dr. George Tsoflias, Dr. Ross Black, Dr. Leigh Stearns, Dr. JiLu Li and Dr. Cornelis van der Veen). I also like to thank the geophysics students of the Geology Department for their support. Finally, I would like to especially thank my fiancé Betzanim Medina as well as family and friends who stood beside me during my graduate studies.

TABLE OF CONTENT

FIGURE TABLE

1.0 INTRODUCTION

Over the past two decades, remote sensing has provided scientists an unprecedented view of remote locations including the ice sheets in Greenland and Antarctica. Airborne and satellite measurements over the Greenland Ice Sheet have shown that over the last 20 years the speed and discharge of ice has increased significantly (e.g. Rignot and Kanagaratnam, 2006). These observations have heightened the need to better understand the processes that control glacier dynamics and their contribution to rising sea levels (e.g. Luthcke et al., 2006; Rignot et al., 2008; Velicogna, 2009, Rignot, and Kanagaratnam, 2006). Numerical models are used to predict the behavior of ice sheets and glaciers. A comparison of multiple numerical model simulations has revealed that no ice-sheet model could reproduce recent observed rapid changes in ice-sheet elevation and velocity (Bindschadler et al., 2013). One of the challenges faced by ice flow modelers is the lack of data regarding key model parameters, including the nature of the bed under the glacier and physical properties of the ice. Large-scale data sets of ice column properties would allow scientists to constrain and improve numerical flow models. Therefore, developing tools that can map these properties over large areas of the ice sheet is one of the most significant challenges faced by modern glaciology.

Ice aligned at a preferred orientation is about three times softer than ice with crystals oriented randomly (Dahl-Jensen, 1985). To account for this softening effect numerical modelers often introduce enhancement factors that are tuned to obtain agreement between predicted and observed surface velocities (e.g. Seddik et al., 2009; Wang et al., 2012). But ice crystal orientation measurements are only available for a few ice cores. However, most deep ice cores are drilled in areas mostly free from the shear stress parallel to the ice sheet surface that controls deformation in most of the volume of ice sheets and only provide information about the ice at the

drilling site. Therefore, it is necessary to develop techniques to describe ice fabrics using remote sensing methods covering large areas. This would provide modelers information on the spatial variability in enhancement factors over large regions or the entire ice sheets. For this investigation, I used a combination of radar and seismic measurements collected near the NEEM ice core to detect the presence of preferred ice crystal orientation for a 100 km^2 region. The results of the analysis were compared to the NEEM ice core crystal orientation and electrical resistivity measurements in order to establish a direct relationship between the radar and seismic results.

The basal character of an ice sheet or glacier has a significant effect on ice flow. Calculations show that glacier flow can be dominated by processes at the bed especially in areas where deformable layers are present (e.g., Alley 1986; Budd et al., 1984; Alley et al., 1987). Thus, it is reasonable to suppose that ice flow behavior will be different on deforming till as opposed to water-lubricated ice/bed interface (Alley et al., 1987). Given the importance of the basal character to the behavior of ice sheets and glaciers it is necessary to determine the type of material at the ice/bed interface. Gravitational and magnetic measurements collected over Jakobshavn Isbræ suggest that soft bed sliding is the dominant mechanism of fast flow (Block and Bell, 2011). For this investigation, I re-processed a 9 km seismic line collected by Horgan et al., (2008) to determine the thickness and spatial distribution of the sub-glacier material beneath the Jakobshavn catchment region. Using the seismic interpretation, I generated a 2D model of the area in order to test a linearly viscous model to simulate flow and investigate whether the presence of a deforming bed is compatible with observed surface velocities and inferred basal drag. Drag at the base of the glacier can be inferred from surface ice velocity observations

(Joughin, et al., 2010), and this provides the upper boundary condition for a simple model describing sediment (e.g. Van der Veen, 2013).

This dissertation has three objectives:

1) Assess the utility of ground-based seismic and radar methods for detecting the presence of preferred ice crystal orientation near the NEEM ice core site.
2) Use seismic reflection to image the sub-glacier material beneath Jakobshavn Isbrae.
3) Assess whether flow characteristics of Jakobshavn Isbræ inferred from consideration of force balance are compatible with the presence of a layer of deforming sediment.

2.0 CHAPTER I: COMPARISON OF PREFERRED ICE CRYSTAL ORIENTATION DATA AT THE NEEM ICE-CORE SITE WITH MULTI-POLARIZATION RADAR MEASUREMENTS

2.1 CHAPTER I: INTRODUCTION

Accurate modeling of ice flow is of critical importance for understanding the contribution of large ice sheets to sea level change. As a result, scientists and engineers have developed an array of mathematical models and remote sensing technologies to improve our understanding of large ice sheets. Most studies have concentrated on areas of fast flow, where ice flow is mostly controlled by processes occurring at the ice/bed interface (e.g., Van der Veen, 2011). However, ice streams and fast flowing glaciers are fed from inland sources where motion is mostly controlled by ice rheology (Matsuoka et al., 2003) as well as the driving force and the basal drag (Van der Veen, 2013). Studies have shown that ice characterized by crystal orientation fabrics (COF) is about three times softer than ice with crystals oriented randomly (Dahl-Jensen, 1985). Despite acting at the microscopic scale, processes such as fabric evolution and recrystallization affect the large-scale macroscopic behavior of ice masses. Given the importance of COF to ice flow, modelers use enhancement flow factors to incorporate the effects of COF and obtain agreement between modeled and observed surface velocity measurements (e.g. Seddik et al., 2009, Wang et al., 2012). Therefore, it is necessary to obtain information of the variables that affect ice rheology for large areas in order to gain a better understanding of the behavior of the entire ice sheet.

Advances in remote sensing methods have significantly improved our knowledge of the bed topography for large ice sheets. In particular, ice-penetrating radars are powerful tools for observing the internal properties of ice masses (e.g. Robin et al., 1969; Bogorodsky et al., 1985).

There are three major causes of internal ice reflections in radar measurements: 1) Changes in dielectric permittivity due to density (e.g. Paren and Robin, 1975; Clough, 1977); 2) Changes in dielectric permittivity due to COF (e.g. Harrison, 1973; Fujita et al., 1993); and 3) Changes in electrical conductivity due to acidity (e.g. Millar, 1982; Moore, 1988; Moore and Fujita, 1993; Matsuoka et al., 1996). The power reflection coefficient due to electrical conductivity changes is dependent on radar frequency and ice temperature (Fujita and Mae, 1994). For this reason dual frequency radars have been developed to differentiate reflections caused by COF (not affected by radar frequency), density and ice temperature (affected by radar frequency). However, the vast majority of large-scale radar data sets are collected in a grid pattern and have been acquired using a single center frequency and a bandwidth usually not exceeding 30 MHz. For this reason, it is necessary to develop a simple method that allows the extraction of COF information from single center frequency grid radar data.

The refractive index of single ice crystals is 1.1% larger along the crystal c axis when compared to the other axes (Matsuoka et al., 1997). Therefore, the backscatter power response is dependent on the polarization of the electromagnetic (EM) wave relative to the orientation of the ice crystal. This non-uniform backscatter response due to COF is commonly known as dielectric anisotropy. If we assume that the chemical composition and temperature within individual ice layers is constant for the area of study and with the same radar settings, any backscatter power variation observed between intersecting lines with different antenna orientations must be the result of COF. As a result, it is possible to detect the presence of COF for single frequency radar surveys collected in a grid pattern by comparing the backscatter power of parallel and orthogonal lines at individual layers along the ice column.

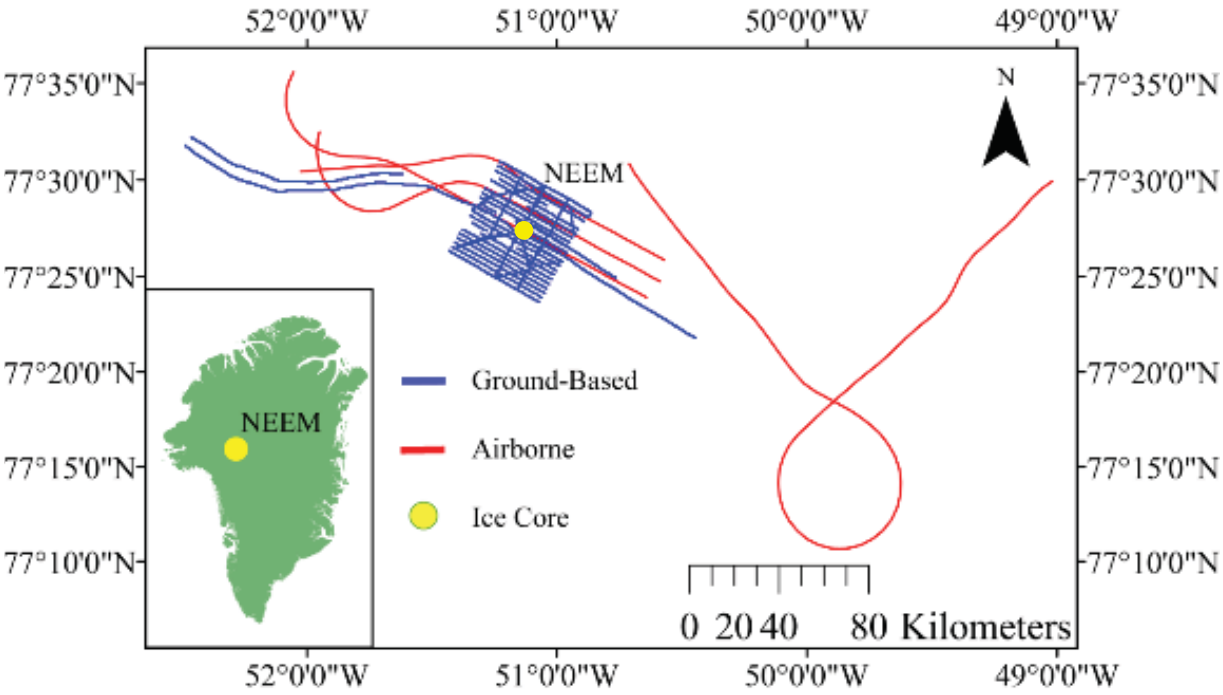

Figure 2.1: Area of study with both airborne (red) and ground-based radar data acquisition around NEEM site.

For this investigation I examine three radar data sets acquired near the North Greenland Eemian Ice Drilling site (Figure 2.1). Two of the data sets were collected in 2008 using a ground-based Multi-Channel Radar Depth sounder (MCRDS) developed by the Center for Remote Sensing of Ice Sheets (CReSIS) and especially configured to extract information about ice column properties. A combination of multi-polarization antenna configurations was used to acquire data in circular and grid patterns. Using the dual polarization circular data and a method developed by Matsuoka et al. (2003), we detected zones where single maxima and disk shape COF patterns are present. The NEEM ice core COF data comparison with the dual-polarization radar interpretation shows good agreement. The backscatter responses at six individual layers were extracted for the entire area of study and reveal strong dependency of backscatter power on antenna orientation for the entire 100-km^2 grid. Comparisons between the dual polarization circular data, the NEEM ice core and the grid lines show that the backscatter power variation observed between the parallel, perpendicular and orthogonal lines can be explained by the presence of COF. The final dataset was collected using the airborne MCRDS system. The data set consisted of three semi linear lines (40 km) and one circular line (12-km diameter). The backscatter responses of three internal layers were extracted from the airborne dataset to determine if a relationship exists between the antenna orientation and the backscatter power.

2.2 AREA OF STUDY

The NEEM ice core is located in northwest Greenland (Figure 2.1). This facility was established to retrieve a complete ice core covering the early Eemian (approximately 115,000 yeas ago) and reconstruct the temperature record of that era. Radar surveys collected near NEEM show continuous and undisturbed internal layers to a depth of about 2,200 m, which agree with

ice-core observations (Dahl-Jensen et al., 2013). Below 2,200 m, internal layer amplitude and continuity decreases: undulations and even overturned folds and shearing of basal material are observed. The transition between clear and lower amplitude layers often appears at the interface between ice from the glacial and Eemian periods. Very large differences in ice rheological properties are documented between glacial ice (with crystal sizes of 1.5 mm and a strong preferred vertical c-axis orientation) and interglacial Eemian ice (with crystal sizes of 25 mm and multiple maxima fabrics). The viscosities of these two types of ice differ by a factor of 50–100. The glacial ice deforms very easily while the interglacial ice remains more rigid (Dahl-Jensen et al., 2013). COF measurements are commonly displayed in terms of three eigenvalues, where the combination of each eigenvalue represents an ice fabric (more details in chapter 2.7). Furthermore, centimeter resolution measurements of dielectric permittivity (Figure 2.2A) and electrical conductivity (Figure 2.2B) were collected along the NEEM ice core.

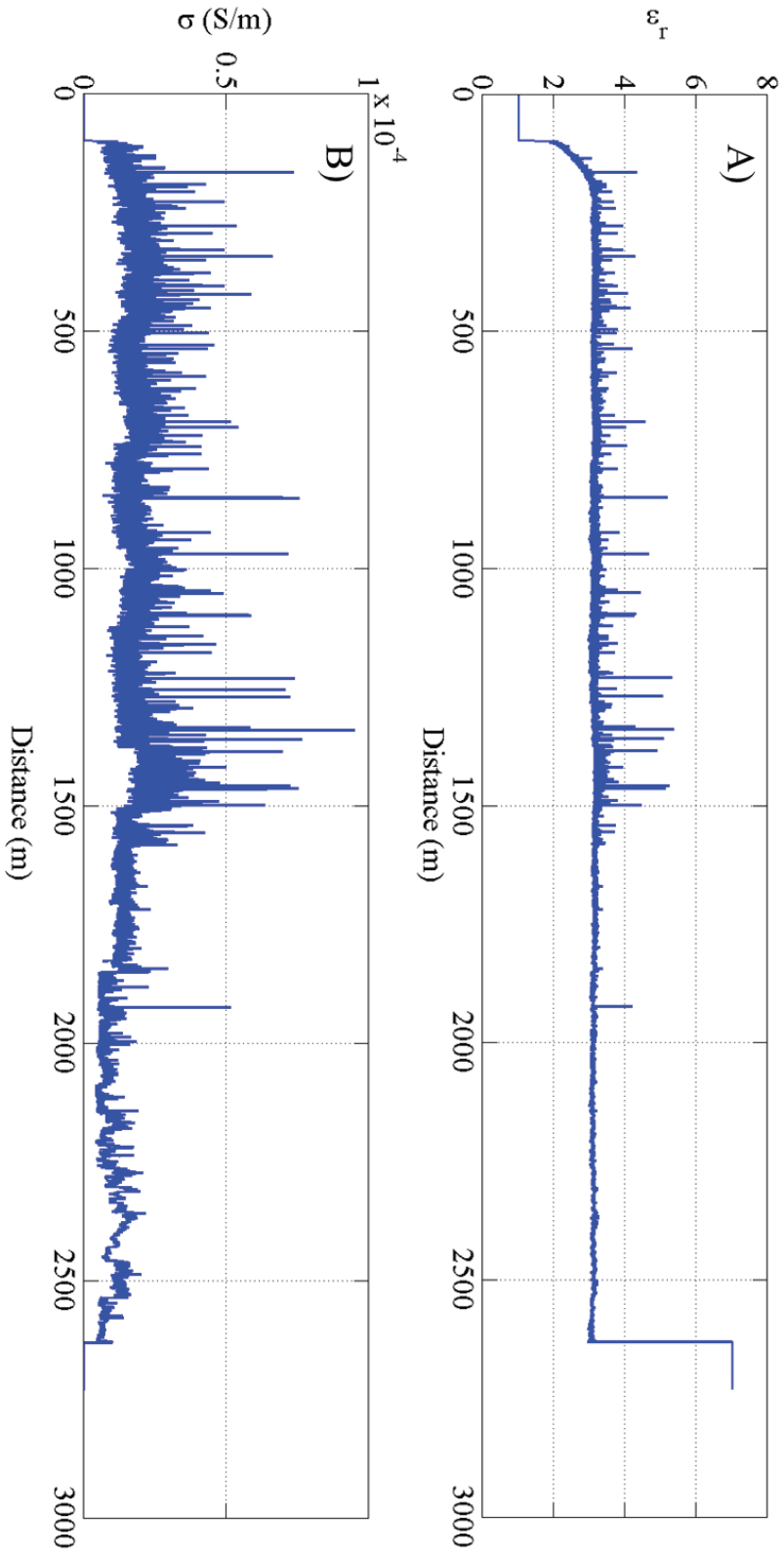

Figure 2.2: A) Dielectric permittivity; B) Electrical conductivity measured in the NEEM ice core (http://www.iceandclimate.nbi.ku.dk/data/).

2.3 DATA ACQUISITION

2.3.1 GROUND BASED DATA

The radar system for both the ground-based and airborne data sets used in this investigation is the Multi-Coherent Radar Depth Sounder (MCRDS) system designed and developed at CReSIS. In the case of the ground-based dataset the antenna arrangement for the survey consisted of two transmitters and eight receivers. The MCRDS system transmitted a linear chirps swept from 135 to 165 MHz. Two antenna configurations were used in data acquisition as shown in Figures 2.3 and 2.4. The first grid data set was collected along twenty 10-km NW-to-SE lines and three 10-km NE-to-SW lines using an E-field co-polarized antenna arrangement (Figure 2.3). The second data set was acquired along a circle of radius of 35 m and lines oblique to the grid data set using two antenna configurations where the two transmitters and eight receivers were arranged in a co-polarized and cross-polarized orientations (Figure 2.4). The antennas were mounted on a sled and pulled at a speed of 5 km/h as shown in Figure 2.5.

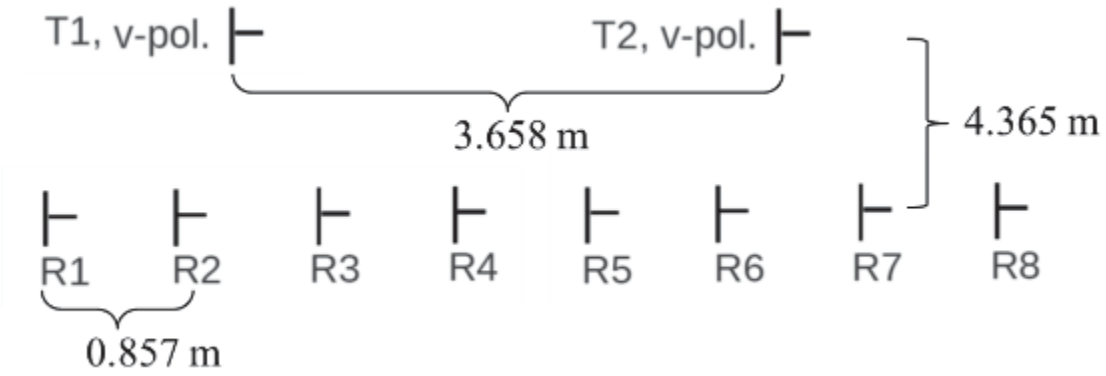

Figure 2.3: Grid data set antenna arrangement. Orientation of transmit (T) and receive (R) antennas. Pulses were transmitted alternatively by T1 and T2

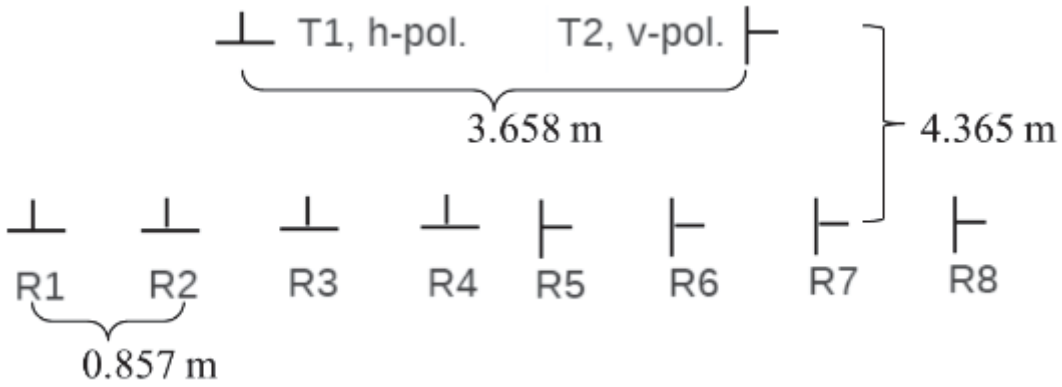

Figure 2.4: Circular data set antenna arrangement. Orientation of transmit (T) and receive (R) antennas. Pulses were transmitted alternatively by T1 and T2.

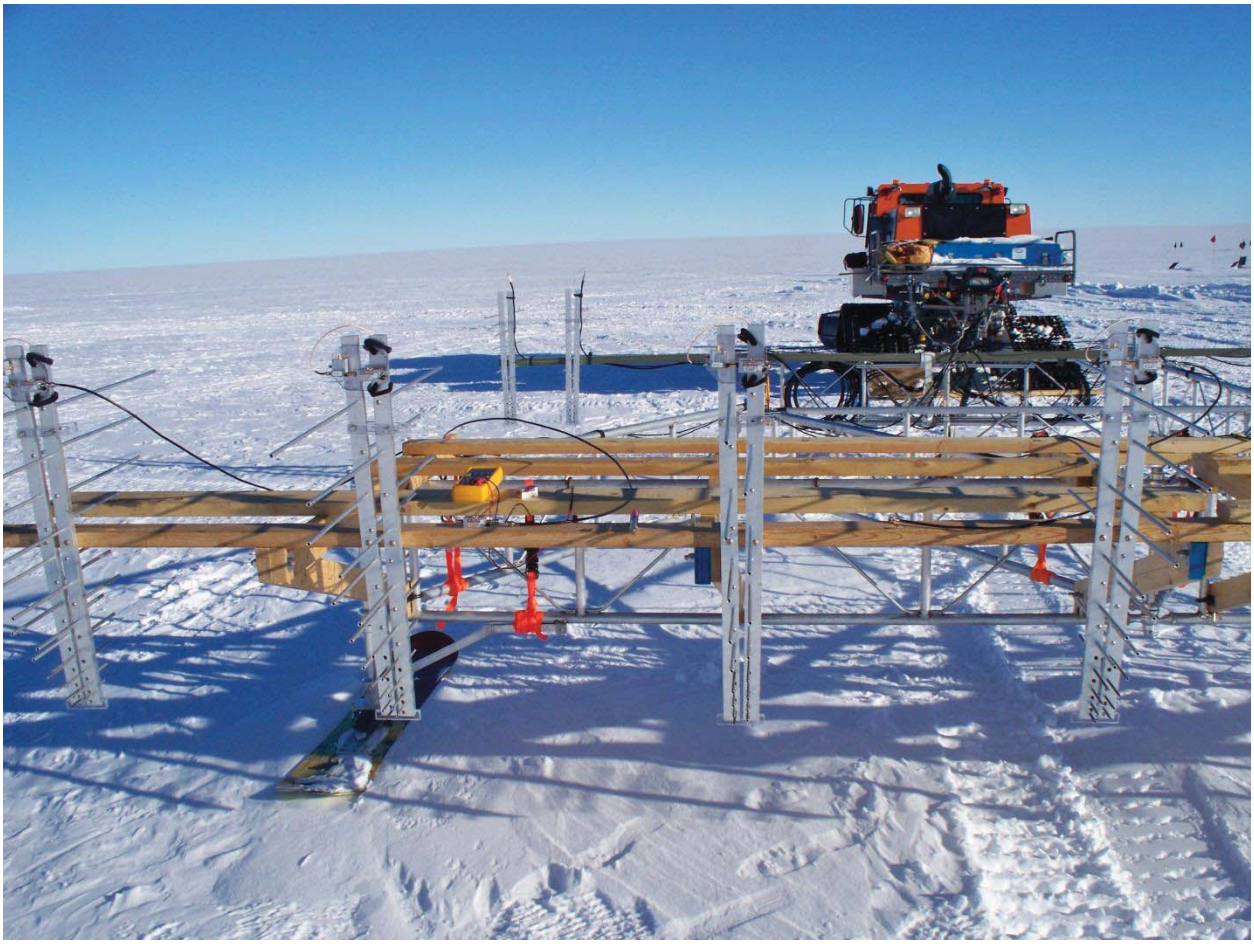

Figure 2.5: MCORDS GPR system mounted on a sled (Photo courtesy of Carl Leuschen: CReSIS).

2.3.2 AIRBORNE DATA ACQUISITION

The MCRDS system used for the airborne data acquisition transmitted a linear chirp swept from 140 to 160 MHz (Li et al., 2012). Six folded dipoles mounted under the starboard wing of the aircraft transmitted this signal with an array gain and a combined peak power of 800 W. Six folded dipoles, identical to the transmit array, were mounted under the port wing of the aircraft. The signals incident on these antennas were digitized individually and recorded to hard drives for post processing. The loop sensitivity of this radar system was around 217 dB with a receiver noise figure of 3.9 dB.

A De Havilland DHC-6, more commonly known as a Twin-Otter, was used as the platform for this airborne radar survey. This aircraft has an average cruise speed of 143 knots with a range of 920 nautical miles. Survey lines were flown at 500 meters above the ice surface. Additional scientific instruments onboard the aircraft included KU-Band altimeter and GPS system. As shown in figure 2.1, three of the lines of the airborne data set were collected over the ground-based NEEM grid survey area while the circular data was collected 50 Km south-east from the NEEM core site.

2.4 GROUND-BASED AND AIRBORNE DATA PROCESSING

Processing of the data from both radar systems includes various procedures in range (range compression), azimuth (F-K migration) and cross-track dimensions (channel combining). These processing steps are meant to increase signal to noise and refocus the energy in to the correct location in space or time (Li et al., 2012). Frequency filtering and pulse compression are the primary steps in range processing. Pulse compression and frequency filtering are done in the

frequency domain to increase the efficiency of processing. A reference copy of the transmitted linear chirp with tapered edges (Ground-Based: 135 to 165 MHz, Airborne: 140 to 160 MHz) is transformed into the frequency domain through fast Fourier Transform (FFT). The raw radar data traces are then converted into the frequency domain and multiplied by the conjugate of the reference chirp. The results are then converted back to the time domain using inverse FFT. Zero padding is applied in time domain to satisfy linear convolution requirements and the acquisition time vector is adjusted according to this padding.

F-K migration is the main component of along-track processing to improve signal to noise ratio, azimuth resolution and to suppress along-track clutter. The motions of the platform including variations in velocity, altitude, heading angles, pitch, roll and yaw have been compensated to satisfy the equal spacing and elevation assumptions of the half-space frequency-wavenumber processing algorithm. Usually the F-K migration adapts a +/- 5-degree nadir looking filter in frequency-wavenumber domain.

Channel combining and beam steering compose the processing steps in cross-track dimension. Recording each of the six receiver array elements individually allows us to perform more dynamic cross-track processing such as Minimum Variance Distortionless Response (MVDR) to reduce cross track clutter (Li et al., 2012). The majority of the data set is combined using a Hanning window. The results from this processing are quality checked to ensure that off-angle returns from the surface do not interfere with the interpretation of the internal layer.

2.5 MULTI-POLARIZATION PLANE TECHNIQUE

The theoretical basis for the multi-polarization technique was first described by Hargreaves, 1977 and successful experiments have been conducted using GPR measurements of

the ice sheets (e.g. Matsuoka et al., 2003; Matsuoka et al., 2012). As mentioned previously, the refractive index of single ice crystals is 1.1% larger along the crystal c axis when compared to the other three crystallographic axes, making ice a birefringent material (Matsuoka et al., 1997). In the case of a birefringent material, the ordinary and extraordinary components of the EM wave split causing a phase differential between both waves. The phase differential causes destructive interference inducing a decrease in backscatter power (amplitude). Therefore, when a linearly polarized antenna transmits a pulse-modulated signal through an ice column characterized by COF, the pulse changes from linearly to elliptically polarized. When the antenna is rotated, the ordinary and extraordinary wave components superimpose either constructively or destructively, depending on their phase difference. This means that the backscatter power will vary depending on the antenna orientation for the same target if COF is present in the ice column (Figure: 2.6). By collecting radar data with two antennas polarized at 90 degrees of each other in a circular pattern and measuring the received backscatter power and phase, it is possible to determine the polarization state of a the EM wave thereby confirming the presence or absence of COF (Figure 2.6).

In the case of disk shape COF patterns (birefringent ice) the phase difference between the magnetic and electric power component response is not zero. The backscatter power varies periodically with the antenna orientation and the amplitude of the variation depends on the phase difference. With single maxima COF patterns (anisotropic ice), the phase difference between the magnetic and electric power component response is zero. The received power varies sinusoidally and the amplitude of variation equals the anisotropy in reflectivity (Matsuoka et al., 2003).

In ice sheets, disk shape and single maxima COF patterns change the polarization state of the EM wave. However, one of the effects of the COF may dominate (Figure 2.6). When the data is collected along the circular pattern (antenna rotation), amplitude extinctions are exhibited every 90 degrees for ice characterized by a disk fabric (Figure 2.6 B). On the other hand, in single maxima COF patterns the reflectivity has one axis of symmetry and amplitude extinctions occur every 180 degrees (Figure 2.6 A). In a transition between the two COF patterns the radar signal either constructively or destructively interfere resulting in a mix amplitude response (Figure 2.6 C). Therefore, we can use the multi-polarization plane technique to discriminate the backscatter response of either birefringent or anisotropic ice (Matsuoka, et al., 2003).

The chemistry within a single ice layer should remain constant assuming the depth of the layer does not change significantly. Therefore, variations in backscatter power within internal layers between orthogonal and perpendicular lines must be the result of COF assuming the acquired radar lines are aligned to the minima and maxima of the extinction pattern. Disk COF patterns exhibit four extinctions while single maxima COF patterns exhibit two extinctions. As a result, disk COF will be easier to detect when compared to single maxima COF for single-frequency grid radar measurements.

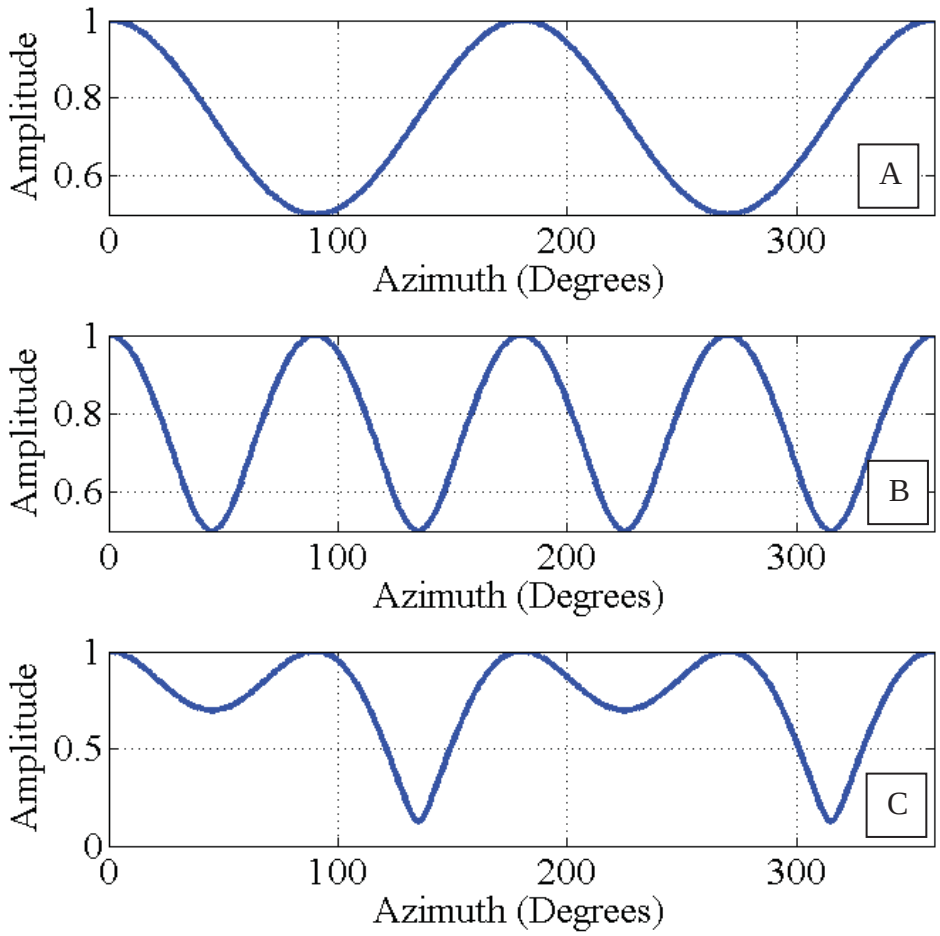

Figure 2.6: Model amplitude response for A) Anisotropic Ice (Single Maxima fabric). B) Birefringent ice (Disk Fabric). C) Transitional zone (Figure modified from Matsuoka et al., 2003).

2.6 RESULTS AND INTERPRETATION

2.6.1 CIRCULAR DATA RESULTS

The ground-based radar data set imaged hundreds of internal layers and the ice bed with along-track spacing of 0.2 m (Figures 2.7A and 2.8A). Close examination of the circular E-field data shows four extinction patterns first appearing at a depth of approximately 370 m (Figure 2.7A-2.8A). The four extinction patterns become well-defined at a depth of 720 m and continue to be apparent to approximately 1500 m (Figure 2.7A). The H-field data (Figure 2.8B-D) set also exhibits four maxima (-140 to -150 dB) but are not as pronounced as the E-field data (-130 to -150 dB: Figure 2.8A-E). A comparison of one extracted layer for both the E and H field shows a phase shift of 30 degrees (Figure 2.8 E). Between 1300 and 1470 m two of the four extinctions begin to curve (Figure 2.7A). Below 1470 m the internal ice reflectivity is dramatically reduced to just a few internal ice layers for both the H and E field data (Figures 2.8A-B). The backscatter extraction for one horizon at 1735 m shows two power maxima (-165 – -172 dB) indicating a pronounce change in the backscatter (Figure 2.7E).

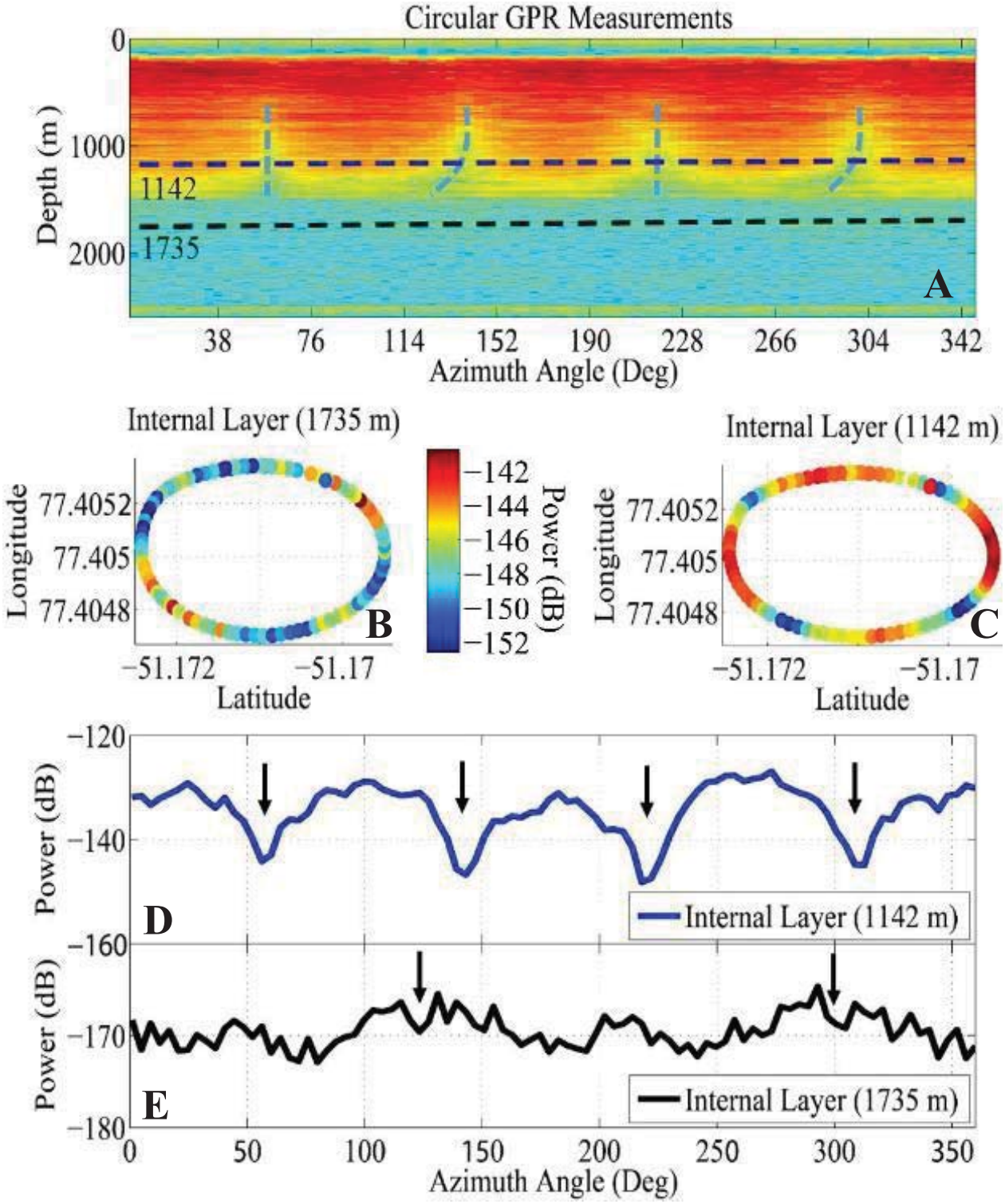

Figure 2.7: Co-polarized radar data collected in a circular pattern. A) Circular data echogram with two interpreted layers at 1142 and 1735 m. Extracted backscatter amplitude corresponding to disk COF of internal layer at 1142 m (C and D) and extracted backscatter amplitude for internal layer at 1735 m corresponding to single maxima COF (B and E).

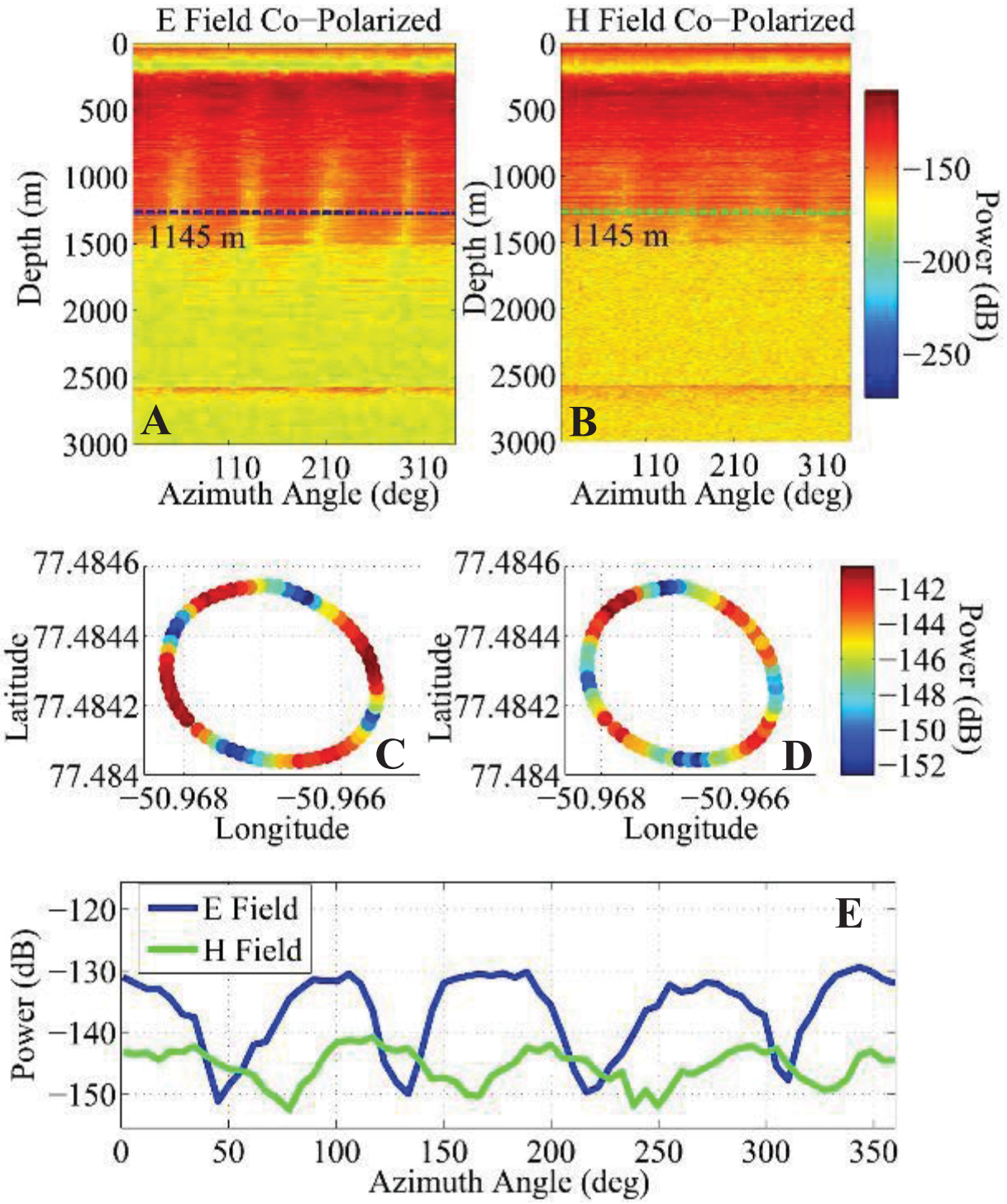

Figure 2.8: Co-polarized radar data acquired in a circular pattern collected using E (A) and H (B) field antenna orientations. Layer extracted at 1142 m for both E (C and E) as well as H field (D-E) antenna orientations.

2.6.2 INTERPRETATION OF CIRCULAR DATA

Based on the work from Hargreaves (1977), the four well-defined extinction patterns observed from 720 to 1500 m (Figure 2.7A and 2.8A), combined with the 30 degree phase shift observed between the H and E field data (Figure 2.8E) indicate that the ice column is characterized by birefringent ice (disk COF) from 720 to 1470 m. From 1280–1500 m two of the four extinction patterns exhibit a 20 degree phase shift (Figure 2.7A). Two of the four minima from the birefringent ice correlate with the two maxima extracted at 1735 m. The maxima response from the birefringent (azimuthal range 90 degrees) and anisotropic (azimuthal range 180 degrees) ice caused constructive interference thus increasing to the backscatter power of two of the four minima (see Figure 2.6 C for model-based example). Given that the azimuthal range from the maxima in the anisotropic ice is 25 degrees larger than the birefringent ice, the discrepancies between both maxima are manifested as a phase shift. Therefore, the zone where two of the four extinctions are shifted is interpreted as a transitional zone between birefringent and isotropic ice. Below 1470 m the internal reflectivity within the ice is reduced dramatically and the ice backscatter response changes to two maxima in one revolution (Figure 2.7E). Therefore the GPR response below 1470 m indicates that for the majority of the ice (1500-2490 m) the ice column becomes electromagnetically constant and that the ice column is characterized by anisotropic ice (single maxima COF). Although the variation in COF was easily detectable by examining the power variation as the antenna was rotated, a comparison between the echogram and the NEEM ice core data (Dahl-Jensen et al., 2013) shows no variation in power response as the result of increased ice crystal size (see chapter 2.6 for more details).

2.6.3 GROUND-BASED GRID DATA RESULTS

The ground-based data set was up-loaded into the IHS software package to track internal layers across the grid. Seven internal layers at different depths were tracked and interpreted for the entire grid (Figure 2.9). The first horizon extracted is located at a mean depth of approximately 682 m. The northeastern section of the survey has a mean backscatter response of -118 dB (± 8 dB) while the southwestern one is -122 dB (±13dB: Figure 2.10). The horizon below that location is approximately 20 m shallower than it is below the south-west side of the survey. Horizon 2 is at approximately 742 m depth and maintains a relatively uniform backscatter power of -118 dB (± 5 dB) independent of antenna orientation for the entire area (Figure 2.11). The backscatter response of Horizons 3-5 (Figures 2.12-2.14) closely resemble one another with the average backscatter power gradually increasing by approximately 10 dB from 870 m to 1168 m. The east-to-west lines have an average backscatter response of -135 dB (± 3 dB) with the exception of one line with an average backscatter power of -125 dB (seventh line from north to south: Figures 2.12-2.16). The north to south lines have an average backscatter response of -123 dB (± 4 dB) while the oblique lines vary between -160 and -112 dB making them the most variable backscatter responses (Figure 2.12-2.14). In the case of Horizon 6 the backscatter response of two of the four oblique lines begin to match with the west-to-east lines (-143 dB ± 2 dB), while the north-to-south lines maintain a 10 dB increase in power (Figure 2.15). Finally, horizon 7 was extracted at a mean depth of 1735 m. East-west lines maintain an average backscatter power of -158 dB while north-south lines maintain an average backscatter of -150 dB (Figure 2.16) with one of the lines exhibiting errors (sixth line from south to north).

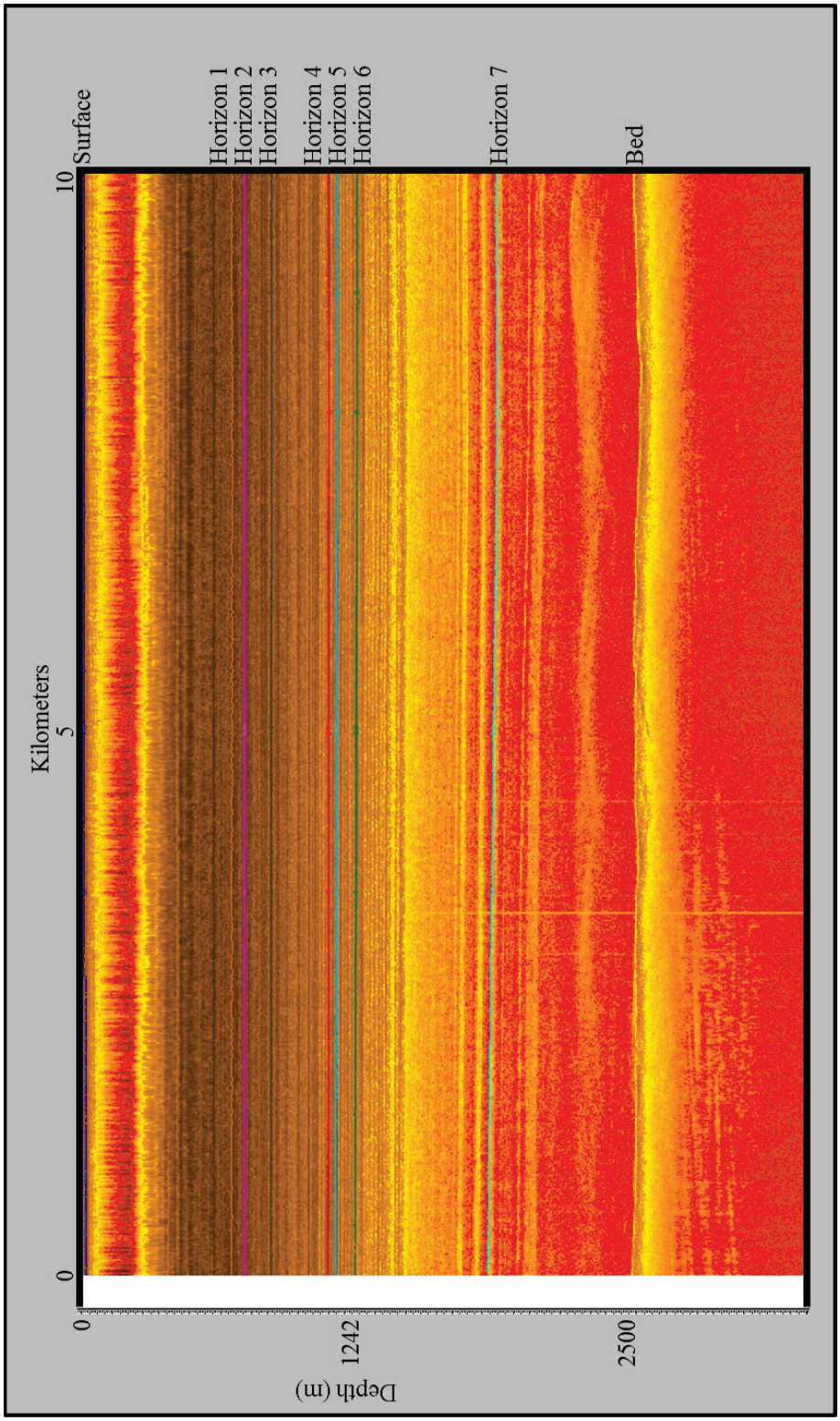

Figure 2.9: Interpreted horizons on ground based data set.

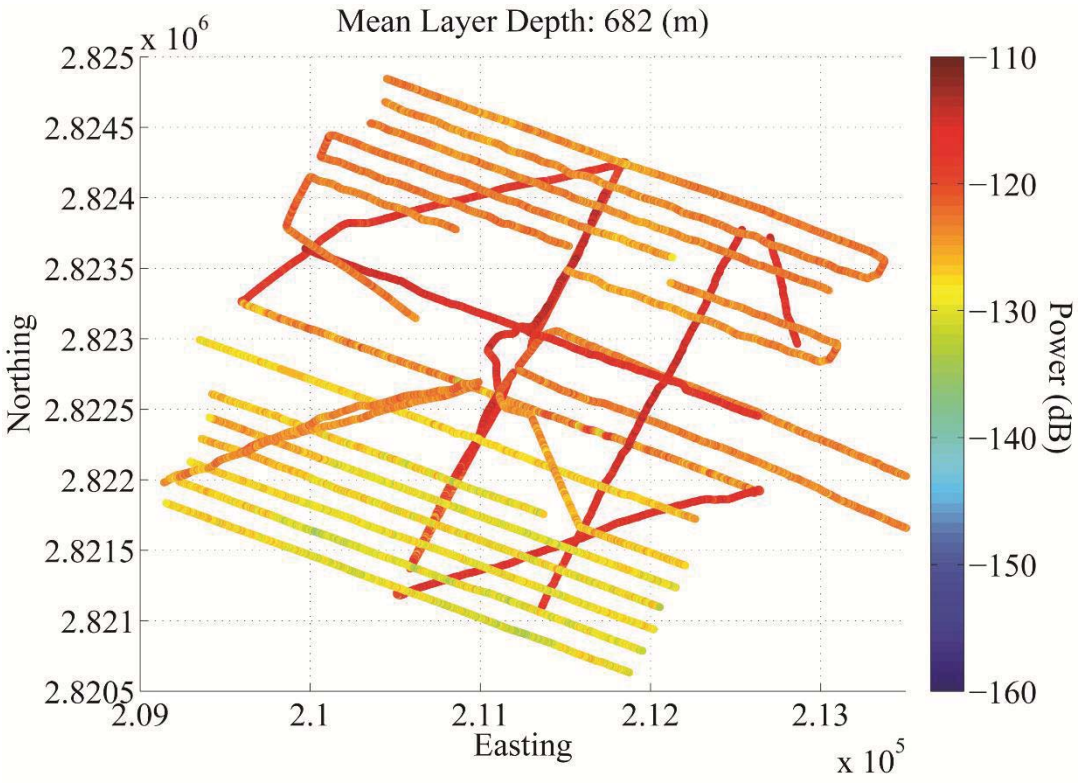

Figure 2.10: Extracted horizon at 682 m (Horizon 1).

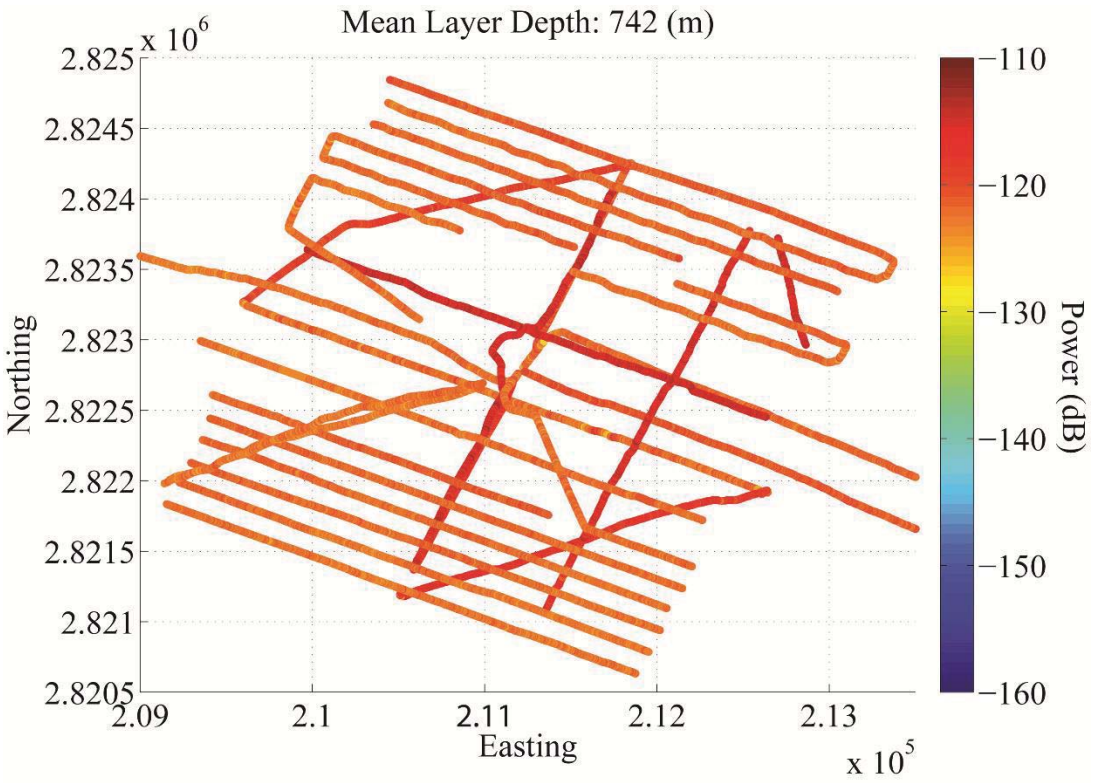

Figure 2.11: Extracted horizon at 742 m (Horizon 2).

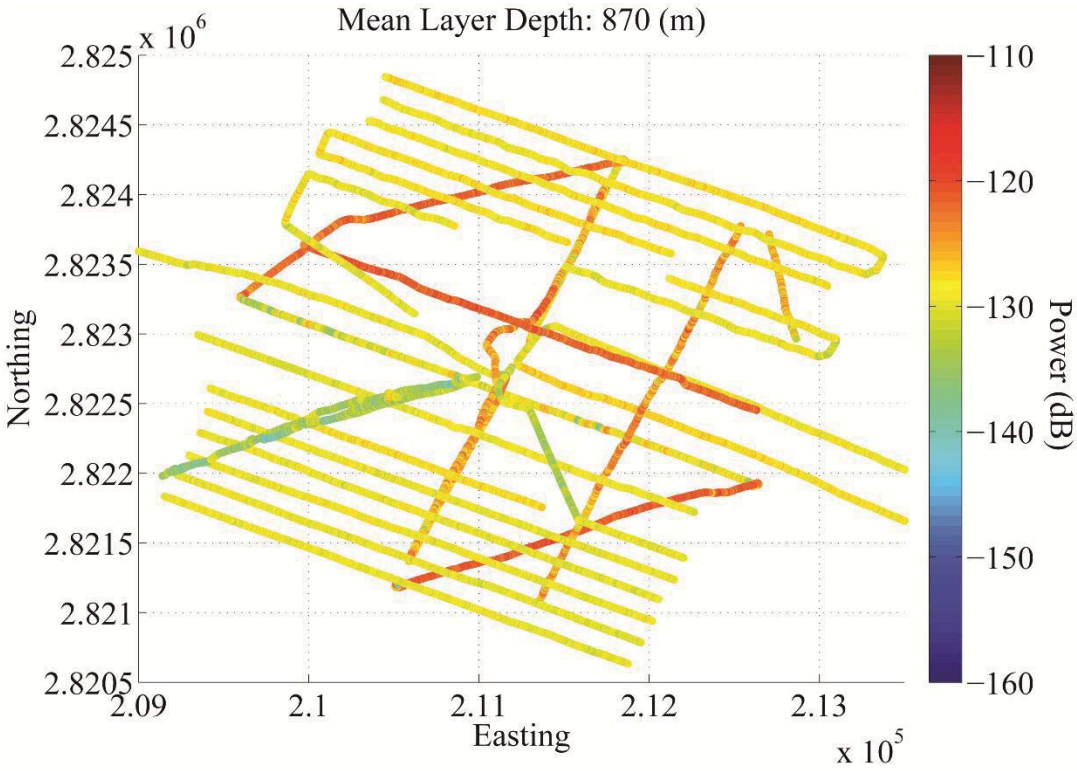

Figure 2.12: Extracted horizon at 870 m (Horizon 3).

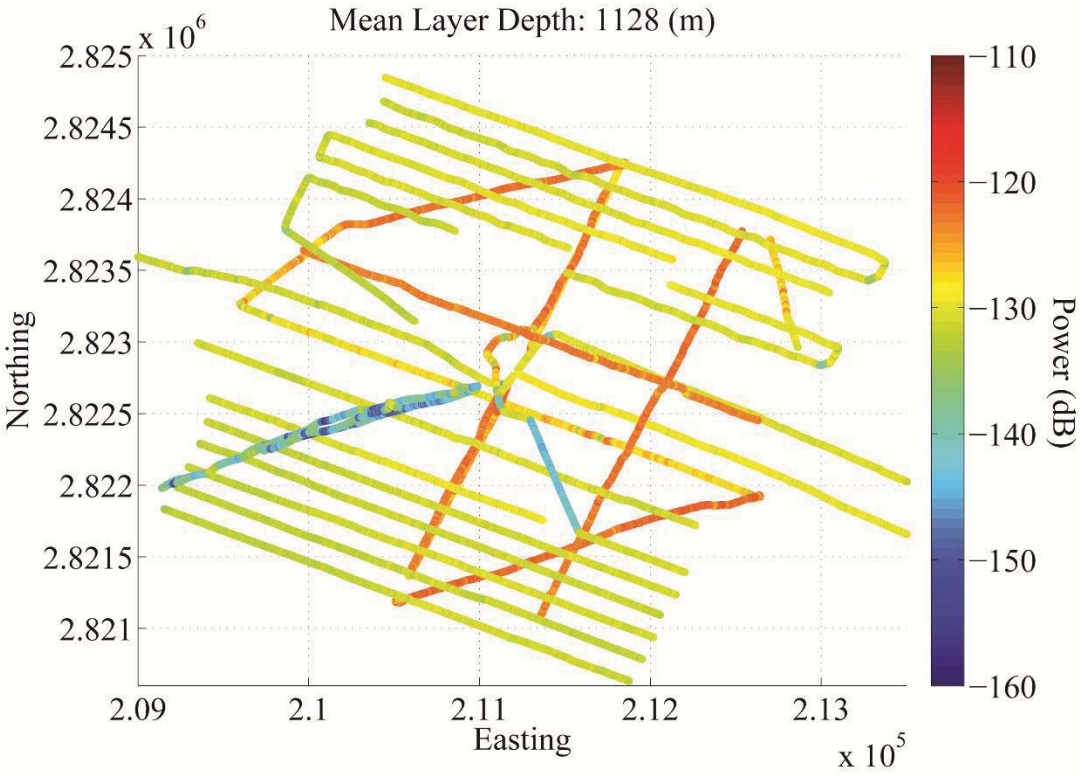

Figure 2.13: Extracted horizon at 1128 m (Horizon 4).

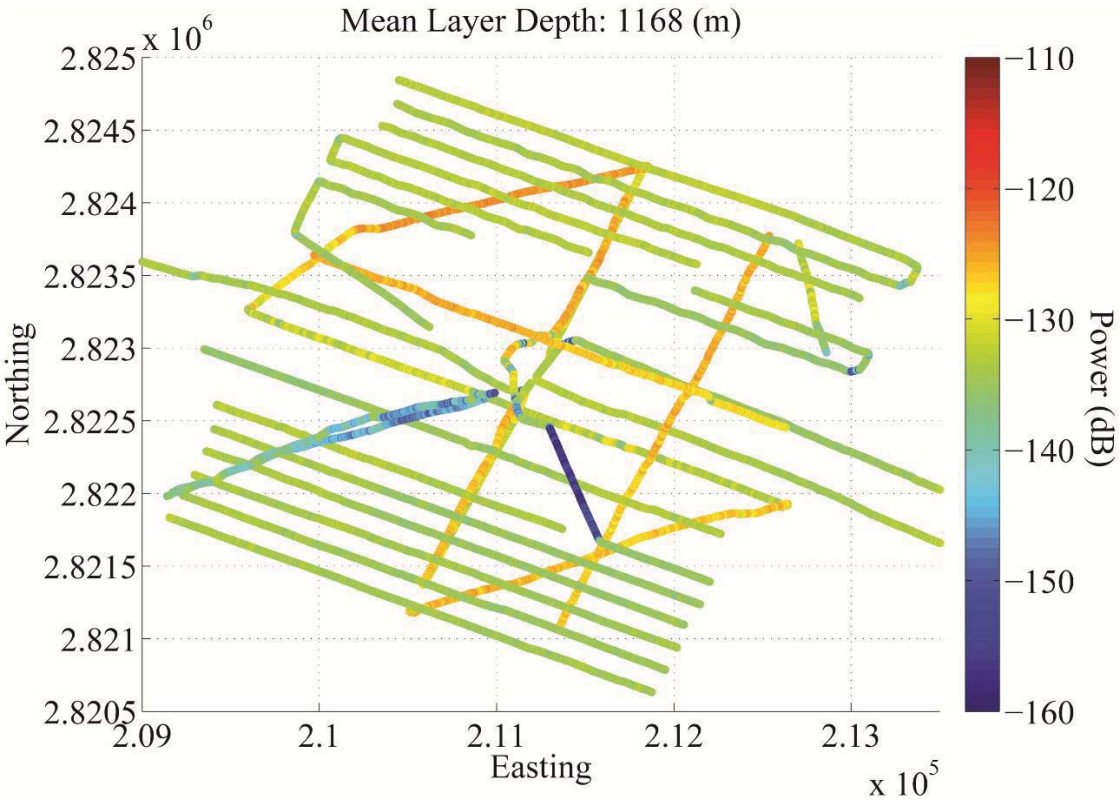

Figure 2.14: Extracted horizon at 1168 m (Horizon 5).

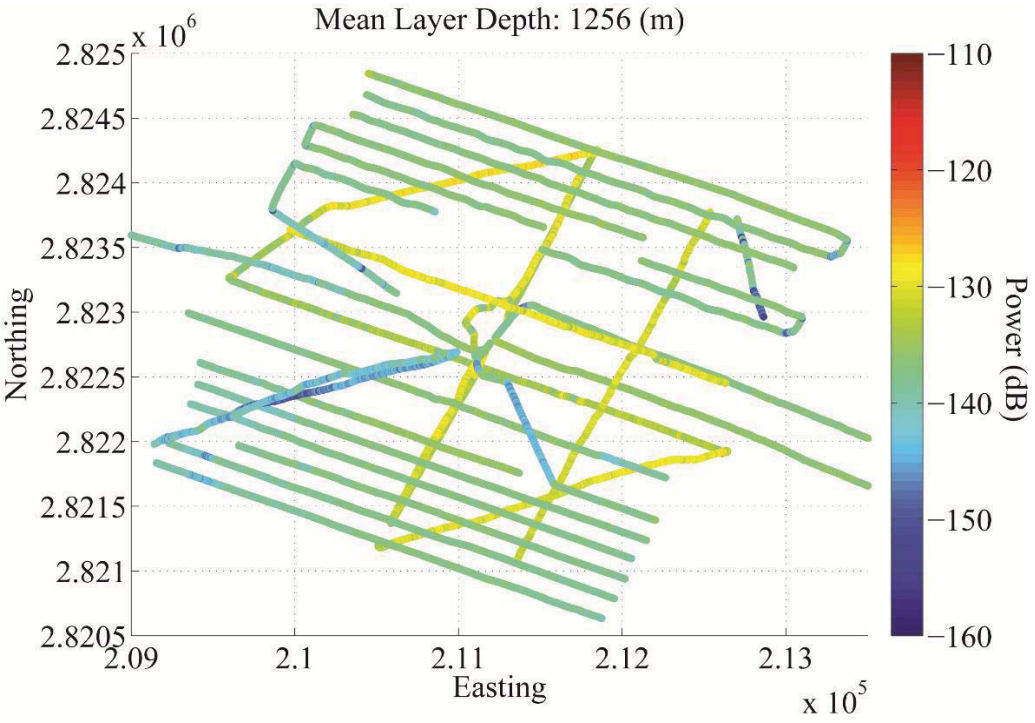

Figure 2.15: Extracted horizon at 1256 m (Horizon 6).

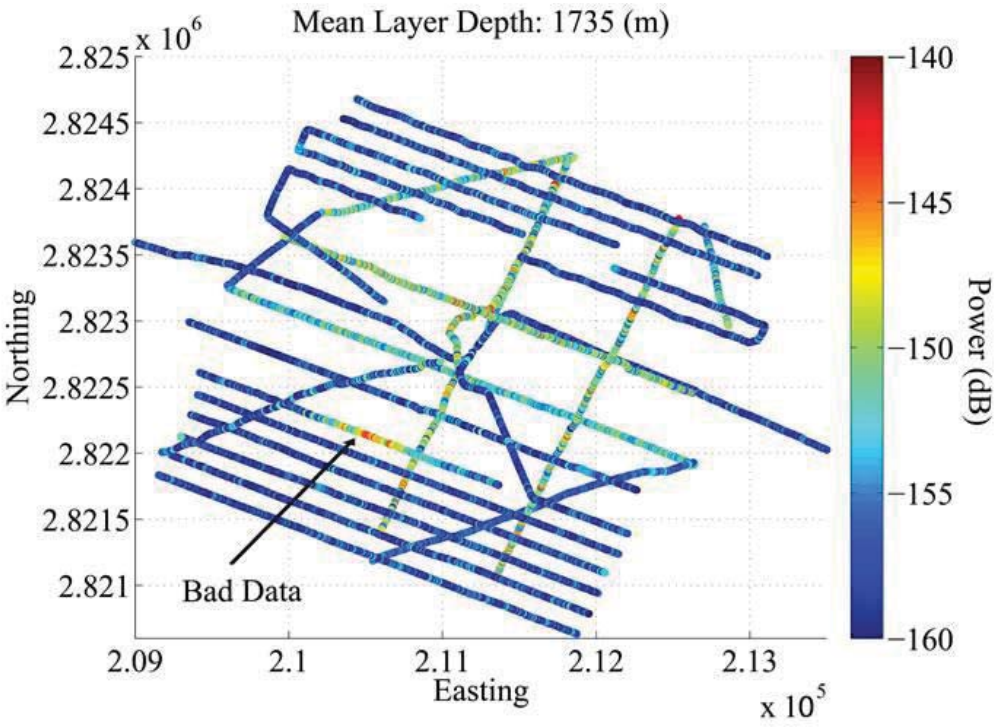

Figure 2.16: Extracted horizon at 1735 m (Horizon 7).

2.6.4 INTERPRETATION OF GROUND-BASED GRID DATA SET

The analysis of the circular data suggests that from 320 m to 700 m the ice column transitions from isotropic ice to birefringent ice (See: Section 2.6.2). Therefore, horizon 1 (682 m) was extracted from the transition zone of the ice column. Horizon 1 deepens by 20 m from north to south of the study area. Close analysis of the radar signal decay shows that the radar attenuates 23 dB per km (Figure 2.10). Therefore, the decay in 6 dB observed in horizon 1 cannot be attributed to the deepening of the layer. Variations of temperature and acidity along the layer for the 100 km^2 area of study are unlikely. Given that horizon 1 is located on the transition zone (random to disk COF) of the ice column, a more likely explanation for the 6 dB power decay from north to south maybe the result of variations in preferred ice crystal orientation within the layer.

Horizon 2 exhibits very little variation in backscatter response for the entire area of study (Figure 2.11). Close examination of the electrical permittivity measurements along the NEEM ice core shows a spike at 742 m (Figure 2.17). The lack of backscatter variability dependent on antenna orientation, coupled with the spike in the electromagnetic permittivity observed in the ice core data, leads to the interpretation that the cause of the Horizon 2 is increased ice acidity within the layer. Horizons 3 and 4 closely follow the same dependency of backscatter power on antenna orientation (Figure 2.12-2.13). As seen in Figure 2.18, small changes in antenna orientation (>5 degrees of azimuth) can have significant changes in the backscatter power especially if the E-Field is oriented in the low- to-high or high-to-low backscatter transition zone (see Figure 2.6 for model based example). Therefore, changes in the along-track heading (5-20 degrees of azimuth) can vary the backscatter power response as much as 25 dB. Figure 2.18 displays magnified sections of Horizon 4 (Figure 2.14) and shows how small changes in along-

track heading (>5 degrees of azimuth) change the backscatter by ±15 dB (Figure 2.18 B). Abrupt changes in along-track heading exceeding 25 degrees of azimuth have rapid changes in backscatter power up to ±25 dB (Figure 2.18 A, C and D). Therefore lines which are not perfectly parallel to each other (>5 azimuthal degrees) may have a variation in backscatter response as seen in Figures 2.18B. Based on the interpretation of the circular data, Horizon 6 is extracted in the transition zone between the disk and single maxima COF (Figure 2.15). As mentioned previously, in the transition zone, two of the four-backscatter maxima decrease in power due to destructive interference (Figure 2.6C). Therefore, the similarity between two of the four oblique lines to the east-west lines is attributed to this decrease in power. Horizon 7 was extracted at a depth of 1745 m (Figure 2.16). The extracted horizon shows a dependency of backscatter power with antenna orientation.

As mentioned previously, the only ice properties that would cause variation in backscatter power, as a function of antenna orientation is birefringence from an ice column characterized by COF. Hence, the backscatter variation between orthogonal lines is about 10 dB and must be the response of COF. Therefore, the detection of single maxima as well as disk COF is possible by observing the backscatter variation between orthogonal lines.

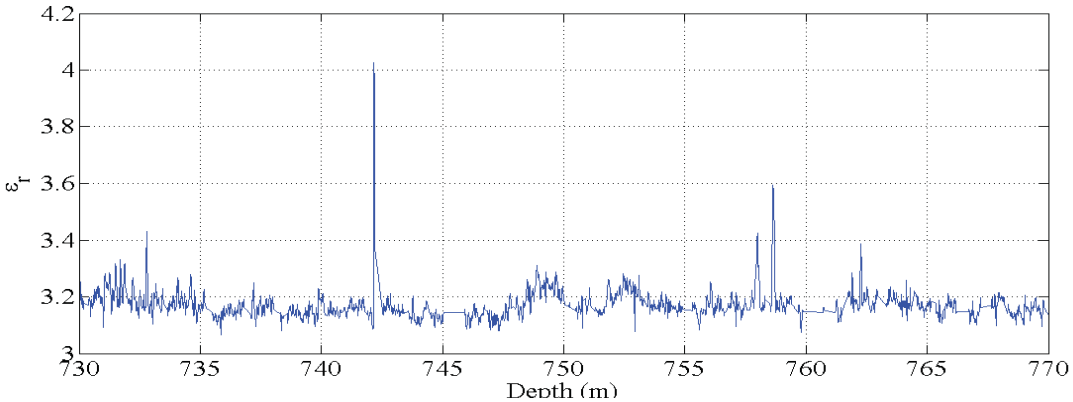

Figure 2.17: Electrical permittivity measured at the NEEM ice core (http://www.iceandclimate.nbi.ku.dk/data/).

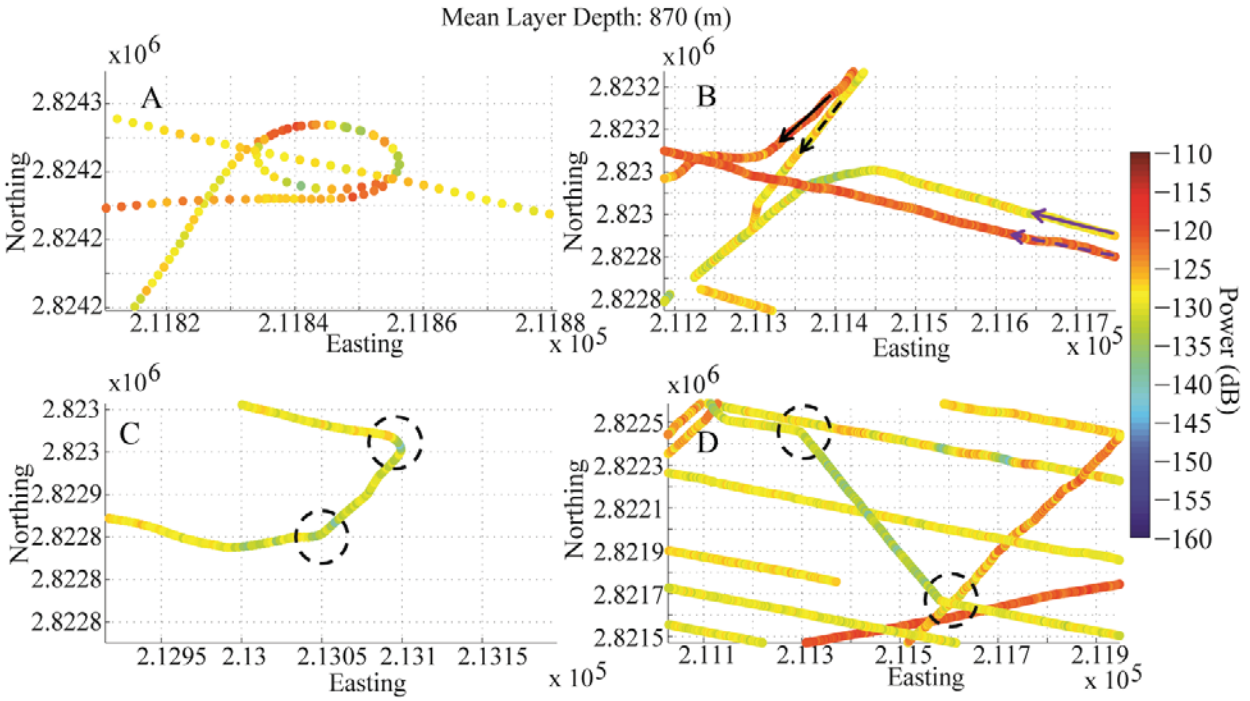

Figure 2.18: Magnified sections of the extracted horizon at 870 m from ground-based GPR measurements: A) Backscatter response of circular data overlaid by east-west line. B) Variation in backscatter as a response of small changes (5-20°) in azimuthal orientation (Purple 10°, Black 15°). C and D: Variation in backscatter as a response of abrupt changes in azimuthal orientation (>20°).

2.6.5 AIRBORNE DATA SET RESULTS

The airborne data set was also uploaded into the IHS software package in order to track internal layers across the grid. The resulting airborne data set consistently shows continuous returns throughout the entire ice volume. However, several vertical amplitude striping events are observed along the airborne data set (Figure 2.19-2.20). The striping correlates with variations in the airplane's elevation, roll, pitch and yaw. Two internal layers were extracted from the birefringent portion of the ice column. Close examination of the horizon reveals variations in backscatter power between -110 and -148 dB (Figure 2.20).

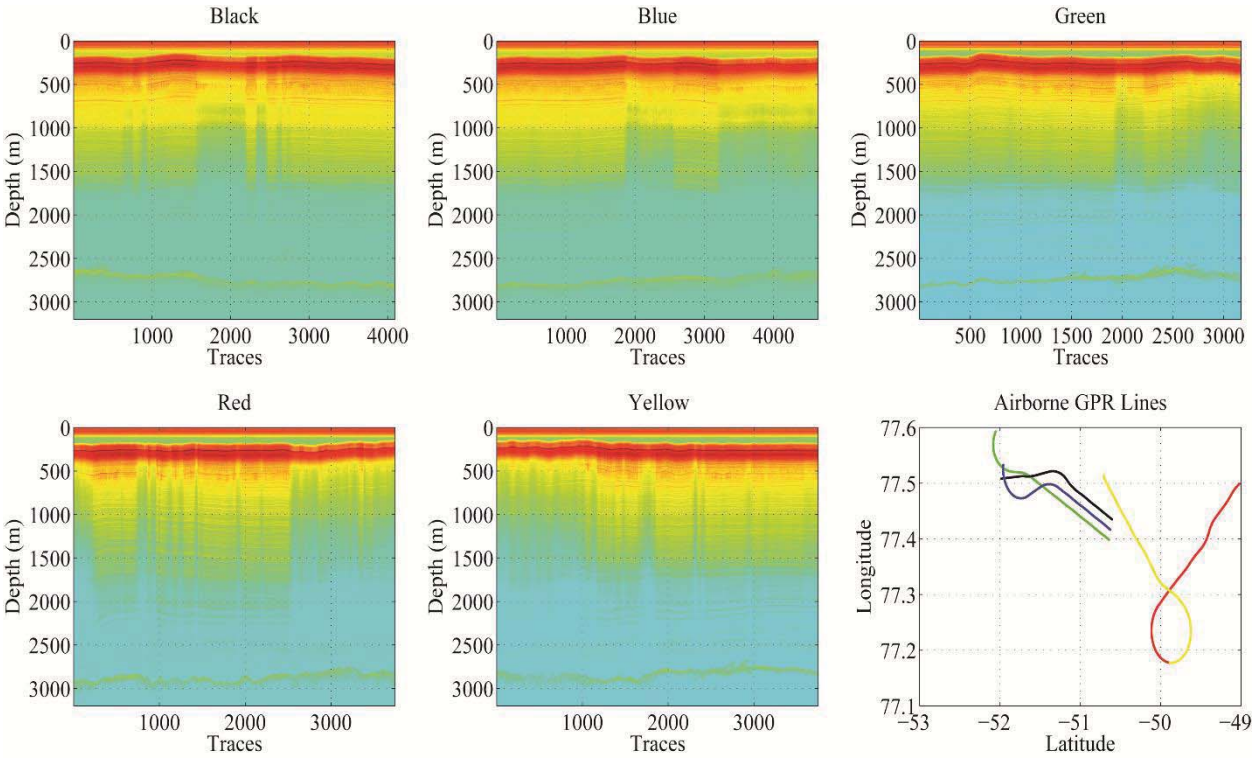

Figure 2.19: Airborne GPR measurements along each flight path.

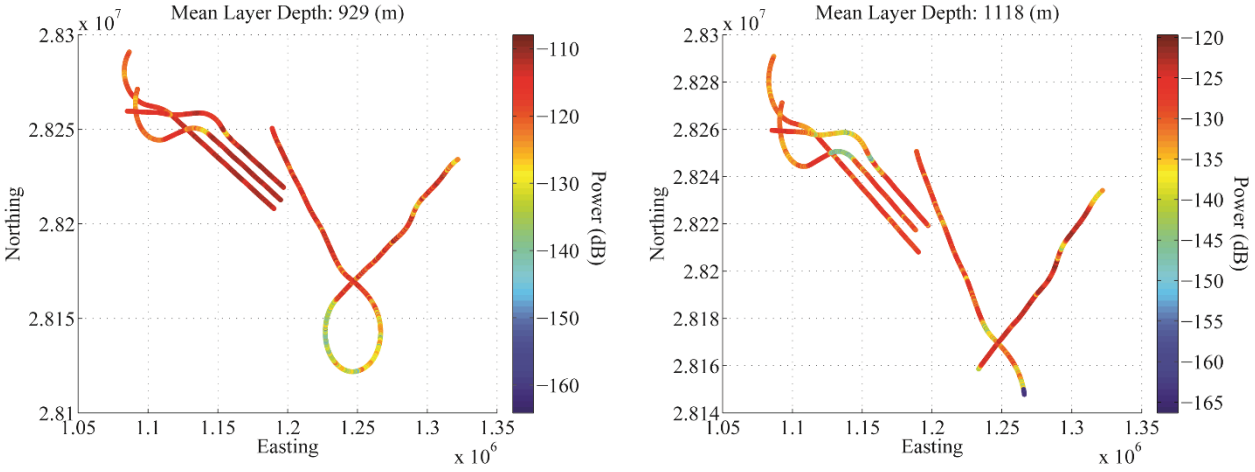

Figure 2.20: Horizon extracted at the birefringent portion of the ice column form airborne data.

2.6.6 INTERPRETATION OF AIRBORNE DATA SET

The CSARP (CReSIS Synthetic Aperture Radar Processor) is a processing algorithm developed at CReSIS (See: Li et al., 2011) which is designed to correct for the challenges faced by data acquisition on airborne platforms (e.g. corrections in elevation, roll, pitch and yaw). One of the challenges faced by scientists and engineers in airborne radar platforms is a spherically spreading wave field. As a result, it is difficult to determine the azimuth and incidence angle of the incoming backscatter. The beam steering technique is used in CReSIS radars to focus the energy of the radar pulse directly perpendicular to the airplane. However, processing steps like beam steering are based on the premise that the antenna array is oriented perpendicular to the ice surface, which is not the case when the aircraft is changing heading.

CReSIS has spent decades developing radars which are optimized to image the bed response. As a result, the bed response is clearly imaged for the entire airborne survey area at NEEM. The backscatter response from the extracted horizons fluctuates between -110 to -148 dB and most of the variation is concentrated in sections were the aircraft is changing heading (Figure 2.20). Although, the aircraft motion has been compensated in the CSARP processing, several striping events are still observed in the data (Figure 2.19). Close examination of the striping shows that the extinction begins at the ice surface in the airborne data set, un like the ground-based data set where the extinction patterns commence at 720 m (Figure 2.7-2.8). For this reason, the striping events are probably not the result of changing ice column properties. The interaction between an electromagnetic wave transmitted at a non-vertical orientation and a smooth surface (e.g. ice) may result in a large part of the transmitted power being scattered away from the radar receiver. Thus, the roll of the aircraft during acquisition can significantly reduce the amount of energy recorded by the radar system, resulting in the striping events observed in

the data. Given that the effect of the energy scattering is larger than the birefringent caused by COF, it was not possible to discriminate between extinction caused by COF and data acquisition effects using this dataset.

2.7 COMPARISON BETWEEN GROUND-BASED RADAR DATA SET AND ICE CORE MEASUREMENTS

The NEEM ice fabric data were measured in the field, at the NEEM camp, during field seasons 2009 to 2011. Measurements were performed on the core from 33m to 2461m depth at an interval of 10m. The raw fabric data were obtained using two automatic ice texture analyzers (AITA). Two versions of AITA were used to obtain the c-axis orientation information. The AITA provided c-axis orientations from thin sections of dimensions up to 12×12 cm^2, at a resolution of 43 μm length for the season 2009, and of 20 μm length for the season 2010. Orientation measurements were provided together with a quality factor that enabled the elimination of sample areas with too much uncertainty, such as grain boundaries. A threshold value for this quality factor was chosen at 70% for all the thin sections studied (see Montagnat, et al., 2014 for more information).

The ice crystal information from the NEEM ice core was provided by Montagnat, et al., (2014), and obtained by determining the second-order orientation tensor a and its eigenvalues. The three eigenvalues a^1, a^2 and a^3 are used to determine the type of fabric present in the ice column by the relation:

$$a^1 \approx a^2 \approx a^3 \approx \text{ 1⁄3⁄ Isotropic}$$

$$a^1 \approx 1 \text{ and } a^2 \approx a^3 < \frac{1}{3} \text{ Single Maxima}$$

$$a^1 \approx a^2 \geq \frac{1}{3} \text{ and } a^3 < \text{ 1⁄3⁄ Disk Fabric}$$

Figure 2.21 shows a direct comparison between the GPR ground based circular data and the three eigenvalues obtained from the NEEM ice core. Results from the ice core show mean eigenvalues of 0.55 for a^1 and 0.22 for $a^2$and a^3 between 0 and 370 m which mostly corresponds to isotropic ice fabric. From 370 m to 720 m a^2 and a^3 start to diverge while, a^1 remains constant. These changes in the eigenvalues correlate with the four faint bands in the GPR circular data, re-enforcing the interpretation of the transition zone between isotropic ice and anisotropic ice from 370 to 712 m. From 720 m and 1280 m the four extinction patterns become well defined and a^2 as well as a^3 diverge by approximately 0.1. The curvature of two of the four extinction patterns was interpreted as the transition between disc fabric and single maxima between 1280 m to 1500 m (see chapter 2.6.2 for details). In this section, a^3 decreases to less than 0.1 while a^2 is approximately 0.2 and $a^1 = 0.75$. Below 1500 m the eigenvalues a^2 as well as a^3 rapidly decrease to less than 0.05 while a^1 increase to 0.95 indicating the presence of a single maxima fabric. At 2200 m the ice crystals increase size and the orientation measurements become inconclusive. Based on the direct comparison between the circular ground base GPR measurements and the NEEM ice core measurements we can determine a good agreement between the radar interpretation and the ice core observations.

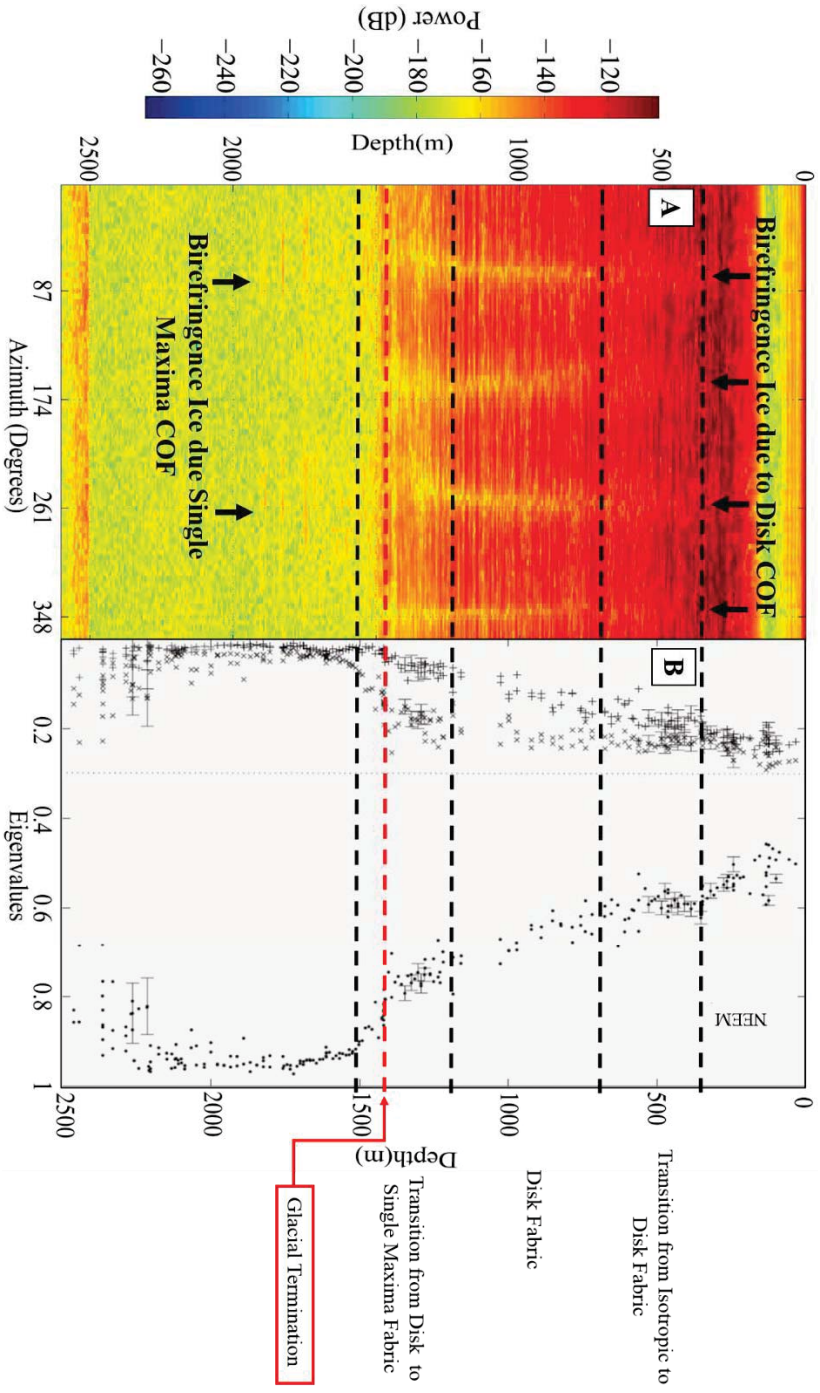

Figure 2.21: A) Ground based circular GPR dataset compared to NEEM ice core measurements. B) Fabric profile along the NEEM ice core, represented by the eigenvalues of the orientation tensor a (dot: a^1, cross: a^2 , plus: a^3). Error bars were obtained from a relation between the number of grains in the thin section, and the eigenvalues calculated (see Montagnat, et al., 2014).

2.8 CHAPTER I: CONCLUSIONS

A combination of single and multi-polarization radar measurements were used to detect the presence of COF by exploiting the birefringent properties of ice. Close examination of the ground-based circular dataset shows four weak extinction patterns from 320 - 720 m. The four-weak extinctions were interpreted as the transition between random ice crystal orientation and a disk COF pattern. From 720 to 1500 m the four-week extinctions become well defined (Figure 2.7). A comparison between the H and E field shows a 20-degree phase shift (Figure 2.8). The combination of the extinction patterns and the phase shift leads to the conclusion that the ice column is characterized a disk COF pattern from 720 to 1500 m. Two of the four extinction patterns from 1290–1500 m exhibit a 20-degree phase shift and can be interpreted as a COF transition zone. Below 1500 m the internal reflectivity within the ice is reduced dramatically and the ice becomes electromagnetically constant (Figure 2.7). The extraction of one internal layer shows two maxima in one revolution. Therefore, the ice below 1500 m is interpreted as ice with a single maxima COF pattern. The comparison between the ice crystal orientation measurements of the NEEM ice core and the ground-based GPR data yields a very good correlation. The quality of the interpretation is the result of the effectiveness of the method presented by Matsuoka et al., 2003 and the high quality of the data collected by the MCORDS radar. This is the first documented example of three different COF (random, disk and single maxima) and their respective transition zones imaged using GPR measurements.

The analysis of the NEEM ground-based grid data set reveals a definite dependency between the backscatter power for six of the seven internal layers interpreted in this investigation. In the case of Layer 2 (742 m) no dependency is observed between the backscatter

power and antenna orientation (Figure 2.11). Close examination between the ice core data and the radar data reveals that the internal layer was the result of increased ice acidity. The backscatter dependency on antenna orientation seen in the remaining six layers is interpreted as the result of COF. The analysis shows that changes in azimuth (> 5 degrees) could result in a ± 25-dB difference in backscatter power, demonstrating the sensitivity of the method. The method is effective in the detection of both single maxima and disk COF. Therefore, it is possible to discriminate between reflections caused by acidity and COF by observing the backscatter response of ice layers from echograms acquired in varying azimuth angles with single polarization antennas.

The analysis of the airborne dataset shows the several striping events in the echogram (Figure 2.19) result from the roll of the aircraft during data acquisition. The roll effect is larger than the effect of birefringence, therefore, the airborne dataset used in this investigation is not able to detect the presence of COF.

3.0 CHAPTER II: EVIDENCE OF PREFERRED ICE CRYSTAL ORIENTATION AT NEEM ICE DRILLING FACILITY, GREENLAND FROM SEISMIC ANISOTROPY OBSERVATIONS

3.1 CHAPTER II: INTRODUCTION

Observations made over a period of 30 years (1990-2010) show that the Greenland Ice Sheet mass loss has been increasing, reaching 263 ± 30 Gt/y (Csatho et al., 2014). Most studies have concentrated on areas of fast flow, where ice flow is mostly controlled by processes occurring at the ice/bed interface (e.g., Van der Veen, 2011). However, ice streams and fast flowing glaciers are fed from inland sources where motion is mostly controlled by ice rheology (Matsuoka et al., 2003) as well as the driving force and the basal drag (Van der Veen, 2013). Studies have shown that ice characterized by crystal orientation fabrics (COF) is about three times softer than ice with crystals oriented randomly (Dahl-Jensen, 1985). Given the importance of COF to ice flow, modelers use enhancement flow factors in order to incorporate the effects of COF and obtain agreement between modeled and observed surface velocity measurements (e.g. Seddik et al., 2009, Wang et al., 2012). Therefore, it is necessary to obtain information of the variables that affect ice rheology for large areas in order to gain a better understanding of the behavior of the entire ice sheet.

Ice crystals are formed by stacking multiple layers of water molecules arranged in hexagonal rings. These layers are called the basal planes of the crystal, and the normal to the basal plane is called the c-axis or the optical axis of the crystal. Crystal orientation fabric (COF) is the result of shear and compressional or extensional stresses induced on the ice column as a response to flow or loading (Hooke, 1981). Laboratory measurements have shown that glacial ice characterized by COF is three times more deformable than ice with randomly oriented crystalline structures. Therefore, the presence of COF can influence the ice flow behavior of glaciers and ice sheets (Dahl-Jensen, 1985). COF data is typically obtained from ice core measurements.

Ice core drilling presents engineering challenges due to core deviation resulting from ice flow. As a result, ice cores are mostly drilled in areas with horizontal flow like domes and ice divides. However, the areas of most active research in the cryosphere are located in areas of fast flow. Therefore, it is important that we increase our understanding of the extent of COF layers within the ice sheets and areas of fast flow in order to comprehend their effects on large-scale ice-flow processes.

Seismic waves in ice propagate up to 5% faster along the c-axis than perpendicular to the c-axis (Bennett, 1968; Bentley, 1971; Röthlisberger, 1972). Bennett (1968) investigated the propagation of p-waves through mono-crystalline ice and concluded that layers of ice characterized by preferred ice crystal orientation can be treated as a transversely isotropic (TI) medium (See chapter 3.3 for more details). Based on this information Blankenship and Bentley (1987) developed a method to detect the mean c-axis ice crystal orientation within the ice column by exploiting the anisotropic properties of single ice crystals at -10^{o} C using common midpoint seismic measurements.

In order to test the accuracy of the method developed by Blankenship and Bentley (1987) a seismic experiment (Figure 3.1) was conducted 6.5 km north of the NEEM ice core facility (see chapter 2.2 for details of the area of study). By comparing the results of the Blankenship and Bentley analysis to the direct measurements of the NEEM ice core it is possible to determine the accuracy of the method. Additionally, by comparing the results of the NEEM experiment with seismic anisotropy results collected on Jakobshavn (Vélez, 2012) it is possible to compare the COF related anisotropy response from two different ice crystal fabric patterns at two sites.

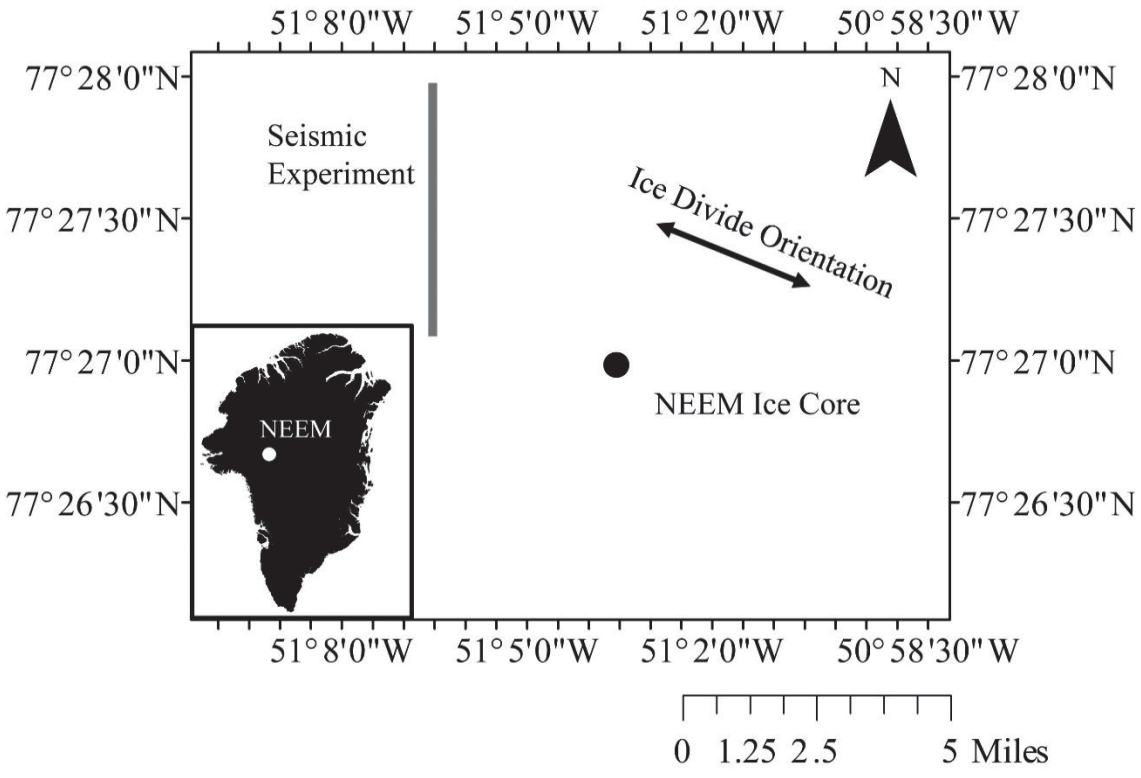

Figure 3.1: Location of seismic anisotropy experiment near the NEEM ice core and orientation of the ice divide.

3.2 CALCULATION OF MEAN ICE CRYSTAL ORIENTATION FROM SEISMIC MEASUREMENTS

The theory of wave propagation through anisotropic bodies is not a common topic of discussion in seismic studies of the cryosphere. Therefore, in this section we will provide a brief overview of the method developed by Blankenship and Bentley (1987). For more information see Bennett (1968) and Blankenship (1982).

A linearly elastic material is defined as one in which each component of stress is linearly dependent upon every component of strain (Nye, 1957). The theory of elasticity of solid anisotropic bodies makes use of the generalized Hooke's law:

$$P_{ij} = C_{ijmn}\varepsilon_{mn} \tag{3.1}$$

where P_{ij} represents nine components of stress, ε_{mn} represents nine components of strain and $C\square ijmn\square$ represents a stiffness tensor that contains eighty-one elastic constants. Given the complexity of the behavior of a medium with a stiffness tensor consisting of eighty-one elastic constants, several tensor symmetries are commonly used to describe the stiffness of a medium and consequently the velocity the wave travels through solids (e.g. isotropic, monoclinic, triclinic, cubic, orthorhombic and transversely isotropic). These symmetries are distinguished from one another by the form of their tensor (Tsvankin, 2005).

Bennett (1968) showed that the type of anisotropy characteristic of hexagonal crystals like ice is similar to that of layered media. A medium of this type is known as transversely isotropic (TI). "TI is the simplest anisotropic case of broad geophysical applicability, it has one distinct direction (usually, but not always, vertical), while the other two directions are equivalent to each other" (Thomsen, 1986). As a result, the elastic properties only vary as a function of the angle from the vertical, i.e. the angle of incidence. A medium of this type has elastic properties

which are radially symmetric with respect to a fixed axis of symmetry. In the case of layered media, the axis of symmetry is normal to the layering. Therefore, if an ice column is composed of ice with COF, the elastic properties of the ice column would be symmetrical normal to the c-axis (Bennett, 1968). The TI tensor contains five independent elastic constants. Bennett (1968) determined five elastic constants for single ice crystals obtained from the Mendenhall Glacier in Alaska (ice temperature:-10° C) by means of ultrasonic measurements. Using the elastic constants, Bennett (1968) modeled the mean slowness (inverse of velocity) of ice crystals at -10° C by assuming that the crystallographic c-axes were spaced evenly along a solid cone of semi-apex angles I with radial symmetry about the Z axes (Figure 3.2). The choice of a solid cone was not random. The geometry of the solid cone is frequently observed in core measurements collected in ice sheets (Blankenship, 1982) where small I angles (closed cone) represent single maxima COF and large I angles represent random ice crystal orientation. The reconstruction of the slowness surface is based on σ, which represents the angle between the axis of symmetry Z and the direction of wave propagation *S* (Figure 3.2). The expression for mean slowness was obtained by spatial averaging the slowness contribution of each single ice crystal orientation as a function of σ. According to Bennett (1968) the expression of a slowness surface on a solid cone for mono-crystalline ice at -10^{o} C is given by:

$$S(\sigma, I) = A + B\cos 2\sigma + C\cos 4\sigma \tag{3.2}$$

$$A = \left\{a - \frac{1}{3}b - \frac{1}{15}c\right\} + \frac{1}{6}\left\{b - \frac{23}{20}c\right\}(\cos I + \cos^2 I) + \frac{9}{40}c(\cos^3 I + \cos^4 I)$$

$$B = \frac{1}{2}(b - c)(\cos I + \cos^2 I) + \frac{1}{2}c(\cos^3 I + \cos^4 I)$$

$$C = -\frac{3}{8}c(\cos I + \cos^2 I) + \frac{7}{8}c(\cos^3 I + \cos^4 I)$$

where a, b, and c are coefficients empirically derived (a=256.28 μs/m, b = -5.08 μs/m, and c = -5.92 μs/m), σ is the angle between the axis of symmetry Z and the direction of wave propagation *S*, and I represents the ice crystal orientation in a conical distribution (Figure 3.2). In figure 3.3, equations (3.2) are used to model the variation of slowness as function of σ for multiple I, where I = 90° represents perfectly random ice crystal orientation (no variation of slowness as a function of sigma: solid line) and I = 0° represents single maxima COF (maximum variation of slowness as a function of sigma: triangles).

The velocity surface can be easily constructed for an ice column from a common mid-point seismic gather if the bed geometry is known for the area of study. Furthermore, the slowness surface as a function of σ can also be determined (Blankenship and Bentley, 1987). By comparing the modelled slowness surfaces (e.g. Figure 3.3) and the slowness surface observed from a CMP seismic experiment it is possible to determine if COF is present in the area of study.

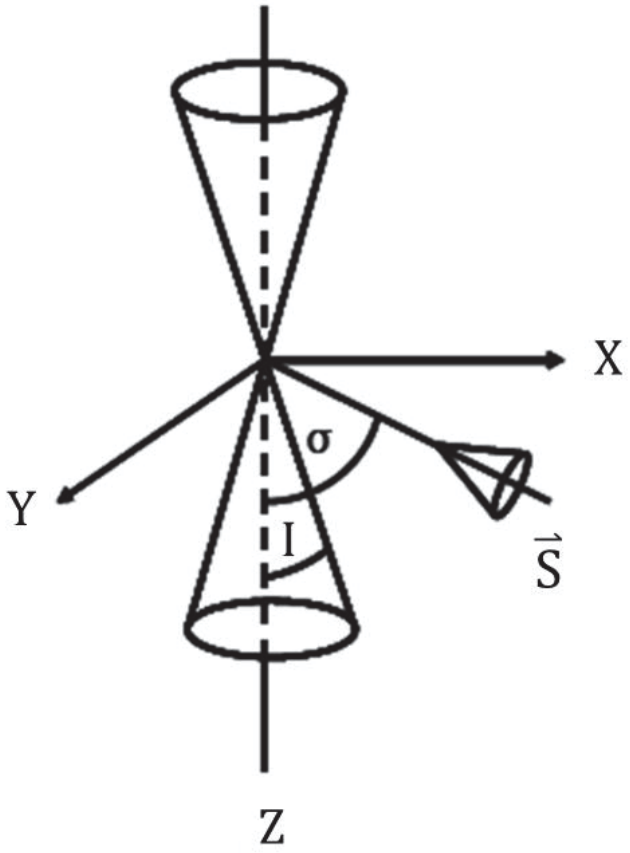

Figure 3.2: Geometry and notation for a conical c-axis distribution (from Blankenship and Bentley, 1987).

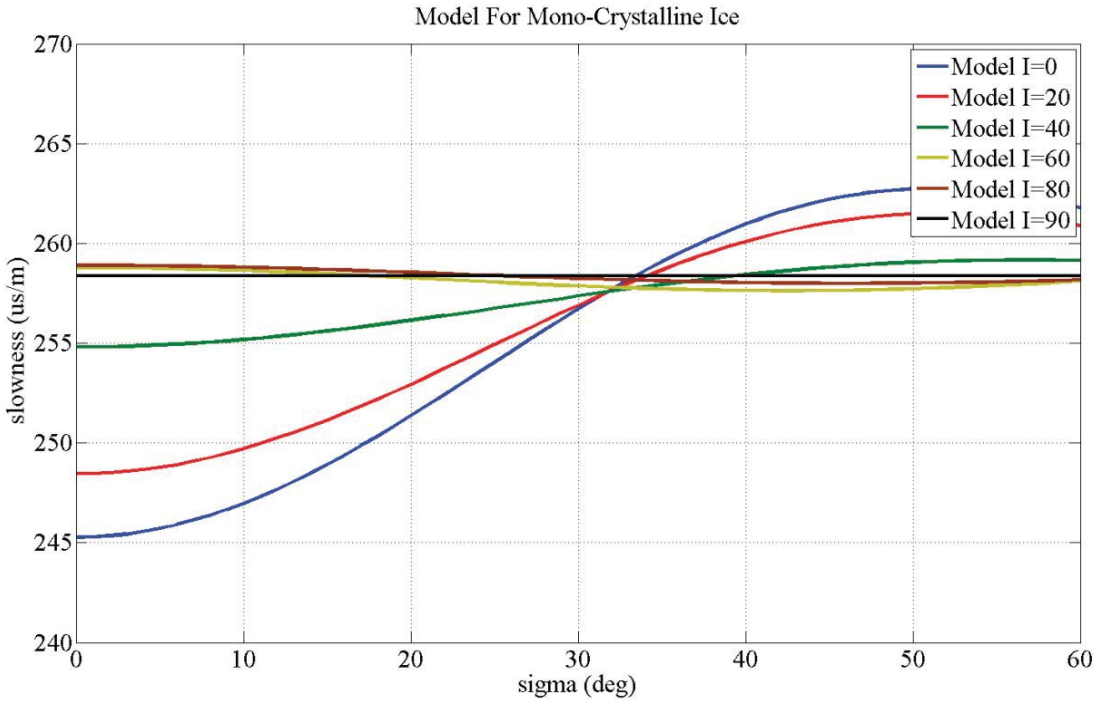

Figure 3.3: Model for slowness surface on a solid cone for mono-crystalline ice at -10^{o} (from Bennett, 1968).

3.3 DATA ACQUISITION

Three source shots with increasing offset were recorded in a pseudo-CMP configuration. Each shot was recorded using a 1900 m long geophone line with ninety-six 100 Hz geophones at 20 m spacing. The first shot offset range was 20 m to 1920 m in order to obtain near offset coverage at small incidence angles. For shots two and three, source locations and receiver locations were rolled 480 m in opposite directions resulting in offset ranges of 1940 - 3840 m and 3860 - 5760 m respectively. Shot records two and three provided wide angle, far offset coverage of approximately twice the thickness of the ice column. The seismic source was 0.5 kilograms of pentaerythritoltetranitrate (PETN) placed in shot holes buried 10 meters below the surface. Data were recorded for eight seconds with a 0.25 millisecond sampling interval using four 24-channel seismographs. Shot triggering and recording was enabled by GPS synchronization.

3.3 EXPERIMENT RESULTS

The analysis presented in Blankenship and Bentley (1987) requires knowledge of the bed geometry (dip angle and depth). I used an average seismic velocity for ice of 3,840 m/s to NMO correct the shot gather based on an ice temperature of -14° C (Rasmussen et al., 2013) and the temperature to p-wave velocity relationship from Kohnen, (1974). As seen in figure 3.4B, the bed reflection is flattened for the first 2/3 of offset range of the shot gather, but moveout remains at far offsets between 1200 to 1920 m. This residual moveout (reflectors at far offsets exhibiting later arrival times) may be the result of bed topography or due to a decrease in seismic velocity caused by the anisotropy in the ice column. The data were filtered using a band pass filter of 80

to 350 Hz in order to increase the signal to noise ratio and facilitate the extraction of time picks for the base of ice (bed) interface.

Assuming a horizontal bed geometry and the time picks extracted from all three shots, the slowness surface was calculated as a function of σ using the Blankenship and Bentley (1987) method. Analysis of the field data shows a slowness variation of 252 to 260 μs/m with σ values ranging from zero to 48 degrees (Figure 3.5). Modeled slowness curves are also shown for I = 30° and I = 32°.Near offset data with σ values of approximately with up to 12° are bounded by model curves for I = 30° and I = 32°. Longer offset slowness analysis results closely match the model I = 30° (Figure 3.5).

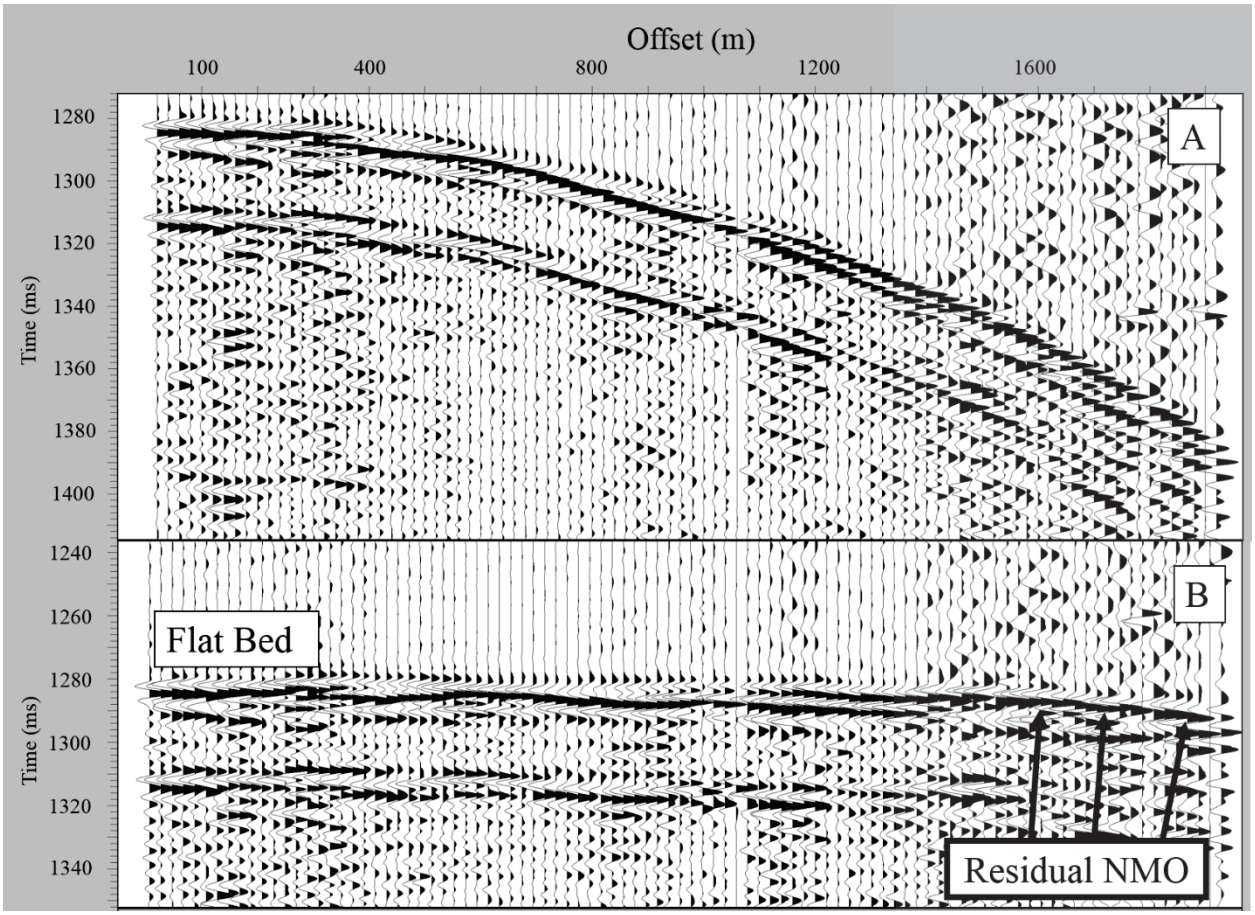

Figure 3.4: Shot one of near-offset data displayed with band pass filter 80-350 Hz: A) Raw filtered data. B) NMO corrected data using ice velocity of 3,840 m/s. The upper reflection (1280 ms) is interpreted to be from the base of ice – top of till interface. The lower reflection (1310 ms) is interpreted as the top of bedrock.

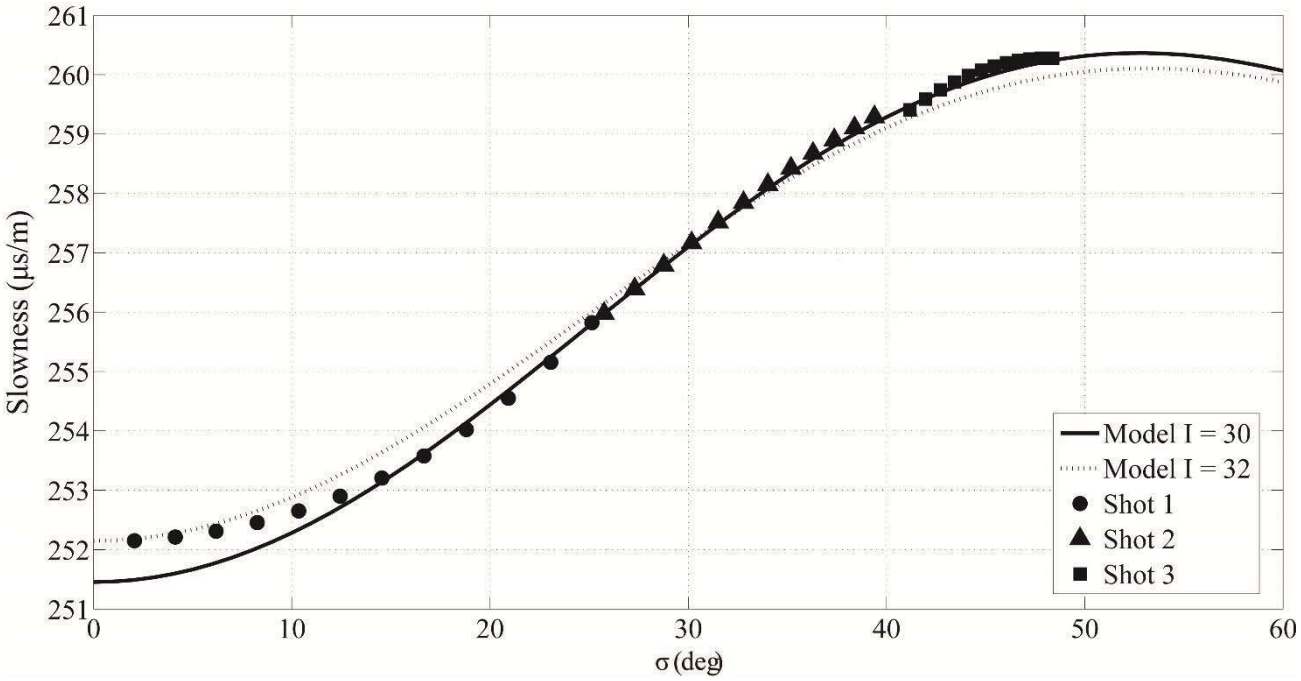

Figure 3.5: Slowness results from Blankenship and Bentley, (1987) analysis for NEEM site showing an I = 30 under a flatbed assumption.

3.4 DISCUSSION

COF measurements are commonly displayed in terms of c-axis orientation and presented in Schmidt plots (Figure 3.6). Schmidt plots (Ferrick and Claffey, 1992) display the relative concentration of the data in one dimension by projecting in the center of the plot the angle between the crystallographic c-axis and the direction normal to the surface. The distribution of the c-axis orientation determines the type of COF (e.g. random, single maxima and disk fabric) and are used to infer information of the stresses acting in the ice column (e.g. Van der Veen and Whillans, 1994). Ice core measurements at NEEM confirmed the presence of COF for approximately 76% (600 to 2500 m depth) of the ice column with 16% of the ice column characterized by single maxima COF and 60% by a disk ice fabric (Montagnat et al., 2014). At NEEM, the transition between random ice and the disk fabric is gradual, changing over an interval approximately 400 m thick. The same behavior is observed in the transition between disk fabric and single maxima over an interval of approximately 220 m. An examination of the seismic data at NEEM reveals no internal ice column reflectivity. The lack of COF seismic reflections is interpreted to be the result of the gradational COF transition, occurring over hundreds of meters, and the relatively short seismic wavelengths (approximately 20 m) of the seismic data.

Although ice measurements are not given in the form of I values, based on the eigenvalues published by Montagnat et al. (2014), I values in the range of 15 to 25 degrees should be expected for the bottom 60% of the ice column. The seismic line was oriented oblique to the northwest-southeast trending ice divide, at about 50 degrees (Figure 3.1). Numerical models of ice deformation show that ice subjected to extensional forces (such as at an ice divide) tend to generate a disk fabric, where the disk is oriented perpendicular to the extensional forces

(e.g. Van der Veen and Whillans, 1994). Given the extensional forces at NEEM, the disk fabrics observed at the area of study should be oriented parallel to the ice divide. As a result, the seismic line is oriented obliquely to the anisotropy of the disk, and the variation of seismic velocity as a function of angle of incidence may not follow a single model of I. This analysis shows that the slowness model of I = 30° fits the mid and far offsets whereas I = 32° fits the near offsets (Figure 3.5). Furthermore, the data acquired in the oblique seismic line measures apparent seismic anisotropy less than the true maximum anisotropy present in ice. It should also be noted that the I estimates are average over the entire propagation path of the seismic wave field, including shallow isotropic ice (I = 90°) and deeper anisotropic ice. The effect of propagation through isotropic ice (24% of travel path at NEEM) results in overall higher I estimates than the COF measurements at the ice core. Therefore, our mean COF I estimates of 30 and 32 degrees are deemed to be in good agreement with localized measurements of 15 to 25 degrees for the bottom of the ice core (Figure 3.5).

Seismic studies have associated the presence of internal ice reflections with sharp transitions in COF (e.g. Horgan et al., 2008; Horgan et al., 2011; Hofstede et al., 2013). However, the experiment performed at NEEM shows that the lack of internal ice reflectivity does not necessarily indicate the absence of COF. The absence of abrupt COF transitions at NEEM is compatible with the location of the site in the interior of the Greenland ice sheet compared to COF patterns that may be expected at faster flowing regions.

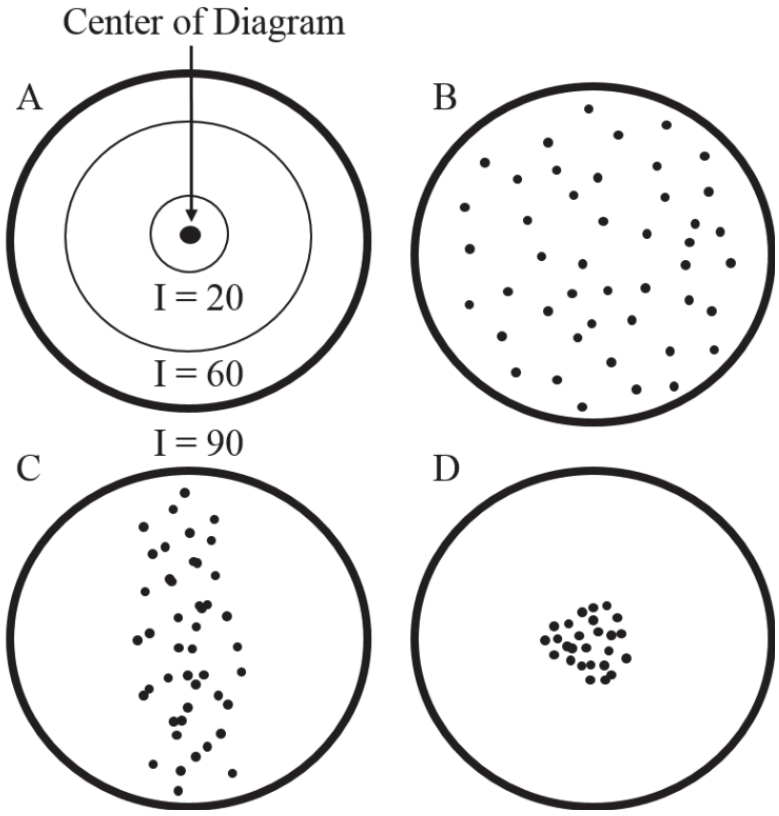

Figure 3.6: A) I angles of 20, 60 and 90 degrees drawn as concentric circles for an ice c-axis conical distribution displayed in a Schmidt plot. Examples of: B) random C) disk, and D) single maxima COF (based on Van der Veen, 1994).

3.5 CHAPTER II: CONCLUSION

Analysis of the seismic wave slowness variability as a function of wave field angle with ice crystal orientation was used successfully at the NEEM site to determine COF. The analysis of the flat bed interface shows a correlation between the slowness results and models of I = 30° to 32° for most of the area of study based on the assumption of a flat bed at a depth of 2540 m. Near offsets vs. far offset slowness observations may fit slightly different I models due to the variation of seismic velocity traveling through different parts of the disc ice fabric as the angle of incidence increases. Given the ice column properties of the area of study, the mean I angle of 30° is considered acceptable and confirms the utility of the Blankenship and Bentley (1987) method for single azimuth data to detect preferred ice crystal orientation. However, because the angle at which the wave front travels relative to the orientation of the disk fabric is not known, a direct one-to-one comparison between the seismic anisotropy analysis and the NEEM ice crystal data is not possible. The use of multi-azimuthal data should substantially increase the robustness of the analysis, thus allowing the comparison between the mean ice crystal orientation based on direct ice crystal measurements and the mean ice crystal orientation based on the seismic anisotropy analysis.

The presence or absence of englacial reflectors also provides an insight in to the nature of the transition between random and anisotropic ice. In the case of the experiment preformed at NEEM, no reflectors were observed in the areas of transition between COF. This is attributed to the thickness of the transition zone (> 100 m). An important observation is that while the presence of englacial reflectivity provides evidence of COF development, the absence of reflectivity does not exclude the presence of COF layers.

4.0 CHAPTER III: SEISMIC IMAGING OF SUB-GLACIAL SEDIMENTS AND ASSESSMENT OF BASAL PROPERTIES AT JAKOBSHAVN ISBRAE, WEST GREENLAND

4.1 CHAPTER III: INTRODUCTION

Observations made over a period of 20 years (1990-2010) have shown that the Greenland ice sheet mass loss has been increasing, reaching 263 ± 30 Gt•y−1 in 2010 (Csatho et al., 2014). These, and many other observations, have raised the concern that in the foreseeable future the contribution of the Greenland Ice Sheet to global sea level may be substantially greater than predicted by ice-sheet models that do not incorporate the physics of rapidly changing outlet glaciers (e.g. Solomon et al., 2007; IPCC, 2014). Therefore, improving the understanding of mechanisms involved in the speed-up of Greenland outlet glaciers is imperative to better constrain predictions of future sea-level rise. One of the most uncertain properties necessary to model glacier flow is strength of the ice-bed interface. Basal resistance can be affected by multiple variables, including presence of subglacial water, sediment viscosity, and sediment layer thickness (Alley et al., 1986; Van der Veen, 2013). Studies have shown that processes at the bed, especially in areas where deformable layers are present, can dominate ice stream flow (e.g., Budd et al., 1984; Alley et al., 1986). Therefore, ice stream behavior may be different over deforming till than on a water-lubricated ice/bed interface (Alley et al., 1987). Given the potential importance that the bed character may have on the behavior of an ice sheet or a glacier, it is necessary to determine the type of material at the ice/bed interface and extract information of variables that can influence ice flow, such as bed topography, the presence of water at the bed, sub-glacial sediment thickness and viscosity.

Seismic reflection profiles have the capability to image sub-glacier sediments (e.g. Blankenship et al., 1987; Smith, 1997; Anandakrishnan et al., 1998; Peters et al., 2006; Smith, 2007). However, challenging field conditions in polar environments typically result in low-fold data acquisition that cannot support traditional CMP based seismic velocity analysis. For this investigation, we present a novel iterative approach for estimating stacking and migration velocities for the geologic materials near the ice/bed interface by exploiting the continuity of the bed reflection. Sub-glacier sediments were imaged below the ice and three facies are identified based on seismic reflector character.

Sub-glacier sediment deformation can account for up to 90% of ice movement (e.g. Alley et al., 1986, 1987). Moreover, the consensus view is that soft sediment is unable to provide large resistance to flow of the glacier through basal drag (e.g. Murray, 1997). However, force-balance estimates at Jakobshavn Isbræ suggest regions of large basal drag (Van der Veen et al., 2011), which would be incompatible with the presence of a deformable weak sedimentary layer. Using the information extracted from the seismic profile (i.e. bed geometry, ice and sub-glacier sediment thicknesses) and satellite based ice flow velocities (Joughin et al., 2010), we investigate the possibility that the sediment layer is actively deforming, adopting a linear viscosity model (Alley et al., 1986; Van der Veen, 2013) and estimating basal drag from the driving stress.

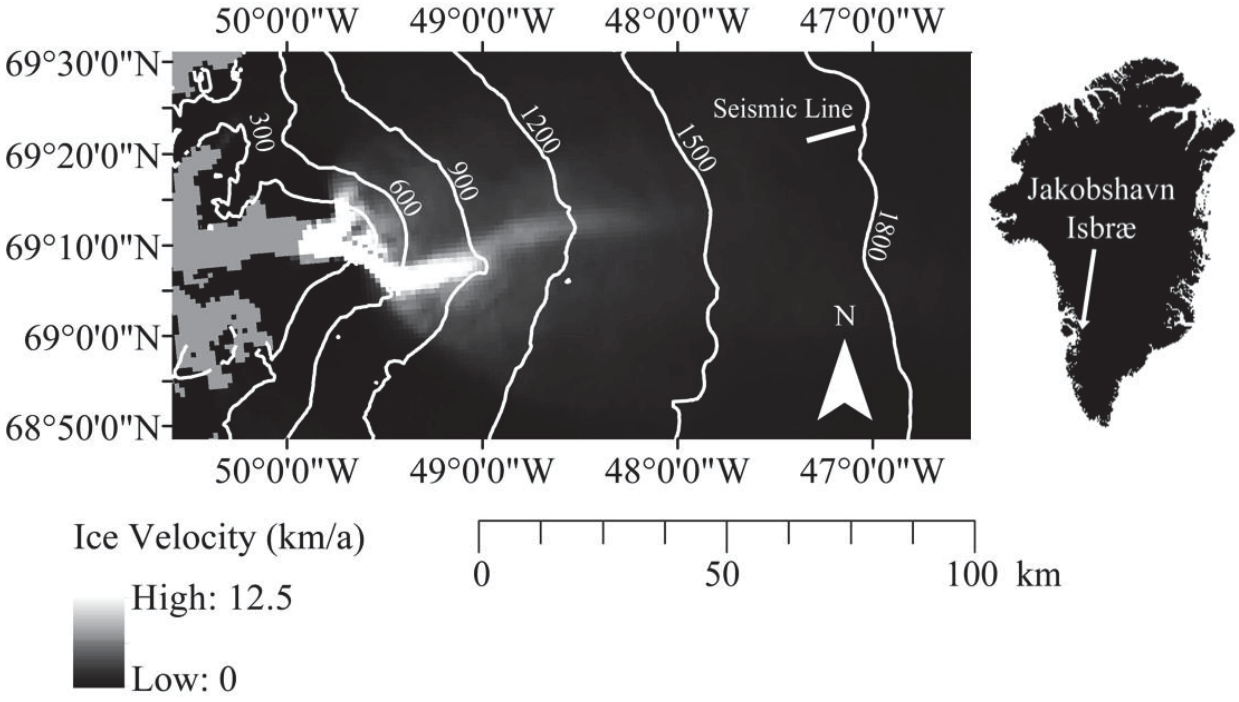

Figure 4.1: Location of seismic profile (dotted line) approximately 100 km from the terminus of Jakobshavn Isbræ. Contours represent ice surface elevation in meters (elevation data provided by CReSIS). Ice flow velocity shown in gray scale (from Joughin, et al., 2010).

4.2 BACKGROUND

Jakobshavn Isbræ (Figure 4.1) is one of the fastest flowing glaciers on earth, and the major discharging outlet glacier in Greenland, draining approximately 7% of the mass of the ice sheet (Csatho et al., 2008). Its flow speed increased from 6 km a^{-1} in 1995 to over 17 km a^{-1} in 2012; additionally, by 2012, the summer speed-up had increased four-fold compared to the 1990s (Joughin et al., 2014). Gravitational and magnetic measurements collected over Jakobshavn Isbræ suggest that the ice/bed interface in the main trunk of the glacier consists of a sediment wedge of up to 2400 m thick that reaches more than 54 km inland of the grounding line (Block and Bell, 2011). Direct core measurements and analysis of seismic data support the presence of sub-glacier sediments, but do not provide estimates of sediment thickness or a geometrical distribution for said layer (Iken et al., 1989; Clarke and Echelmeyer, 1996).

The polar ice sheets are explored using airborne radar soundings which efficiently image ice masses but provide no sub-glacier imaging. Seismic waves have the capability to penetrate below the ice, thus allowing the study of sub-glacier materials. Explosive charges are commonly used as seismic sources in polar environments and km-long geophone lines are deployed in a 2-D acquisition geometry. Seismic data collected in remote Arctic locations tends to be low fold due to the harsh weather, short time duration of field deployments, and the limited size of field crews. Given the low fold nature of seismic data commonly acquired in polar environments it is difficult to estimate subsurface seismic velocities (Smith, 2007) which in turn hinders data processing and the reconstruction of sub-glacier seismic images.

In the special case of seismic studies on ice, it is possible to make assumptions of the material properties in the subsurface since a significant percentage of the seismic profile is composed of a known material (ice). Seismic velocity in ice is mainly affected by density, ice

temperature and preferred crystal orientation, where the p-wave velocity varies from 3740 to 3940 m/s (Kohnen, 1974; Blankenship and Bentley, 1987). Reflection profiling commonly uses an average ice column temperature and the temperature to p-wave velocity relationship published by Kohnen (1974) to estimate ice velocity (e.g., Smith, 1997; Horgan et al., 2008). Another significant advantage of seismic studies conducted on glaciers is the relatively high impedance contrast at the ice/bed interface which is commonly the most prominent feature seen in a seismic profile and is characterized by a strong, continuous reflector.

Close examination of the amplitude and phase of the seismic response at the bed can yield important information about basal properties (e.g. Anandakrishnan, 2003; Smith, 2007). Studies have shown reflected wave polarity reversals introduced by the presence of water at the ice bed interface (Peters et al., 2008) or changes in sediment properties affecting the flow character of the ice sheet, e.g. from basal sliding to deforming bed and vice versa (Smith, 2007).

Previous seismic studies conducted at the same site focused on imaging the bed geometry and determining ice-column properties (Horgan et al., 2008; Peters et al., 2012; Vélez, 2012). They showed that the lower 20% of the ice column is characterized by preferred ice crystal orientation (Horgan et al., 2008; Vélez, 2012) with the ice temperature ranging from -22° C (at 1120 m depth) to approaching 0° C at the bed (Peters et al., 2012), and an average seismic velocity in ice of 3745 m/s (Vélez, 2012). In this study, we re-process the seismic profile presented by Horgan et al. (2008) with the objective of imaging sub-glacier sediments and assessing their impact on glacier flow.

4.3 DATA ACQUISITION AND PROCESSING

The seismic data set used in this investigation was acquired in the summer of 2007 approximately 100 km from the terminus of Jakobshavn Isbræ and consisted of a 9.8 km reflection profile oriented along the flow direction of the glacier (Figure 4.1). Twenty-four 28 Hz vertical-component geophones were deployed at a spacing of 20 m along the receiver line with minimum and maximum shot–receiver offsets of 10 m and 470 m, respectively. The seismic source was 500 g of PETN (pentaerythritoltetranitrate) at a depth of 10 m below the surface. The geophone line and source locations were advanced 160 m, resulting in a maximum fold of two traces. Data were recorded on a Geometrics Geode system with simultaneous shot triggering and data recording enabled by GPS synchronization. Horgan et al. (2008) used the seismic profile to image the ice column which revealed en-glacial reflectivity that was attributed to ice fabric development. In this investigation we reprocess the reflection line to optimize imaging of the section below the base of the ice.

The seismic data acquired at Jakobshavn Isbræ imaged the bed and sub-glacier sediments along most of the 9.8 km 2-D profile. Occasional ice-quakes triggered by the explosive source masked bed reflections due to signal saturation. These traces were eliminated and given the low fold nature of the data, several trace gaps appear on the final processed seismic profile. Most seismic studies in polar environments focus on bed imaging due to the difficulty of imaging sub-glacier reflections using low fold seismic data. However, it is possible to approximate the stacking and migration velocities by using iterative methods. A relatively conventional processing sequence was applied to the data, using a commercial processing software package (Figure 4.2). Initial processing steps included geometry definition, eliminating bad traces, muting

the direct arrival and band-pass filtering (75-375 Hz). Vélez (2012) determined the average seismic velocity in ice at the site location to be 3745 m/s by examining the hyperbolic move-out of internal ice reflections in a coincident multi-offset receiver gather. Given that seismic velocity in ice is unlikely to vary laterally (Smith, 2007) a constant velocity stack was generated using a velocity of 3745 m/s. The constant velocity stack imaged the bed between 0.87 and 1.07 seconds two-way time (approximately 1630 to 2000 m depth). The resulting bed topography was used to define a two layer velocity model, one ice velocity layer and one sub-glacier geology velocity layer. The velocity in ice was kept constant at 3745 m/s while velocities consistent with sub-glacier sediments (Peters et al., 2007) were varied from 2800 to 4000 m/s at 200 m/s intervals. Four sample profiles processed at different velocities are shown in Figure 4.3. Based on the continuity of the bed and shallow sub-glacier reflections, a velocity of 3600 m/s was selected as the sub-glacier sediment stacking and migration velocity.

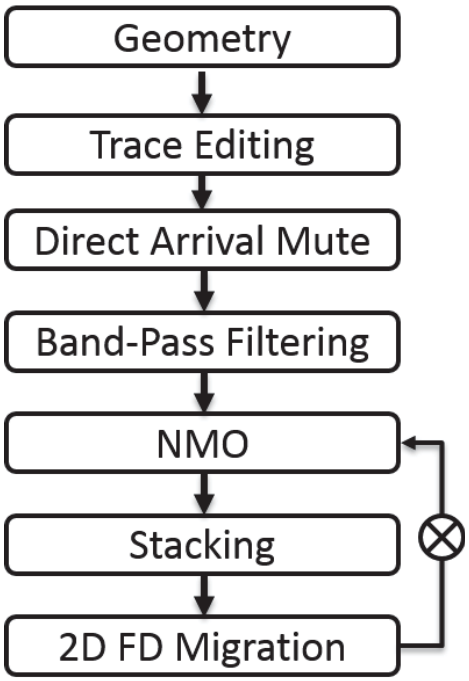

Figure 4.2: Seismic data-processing flow.

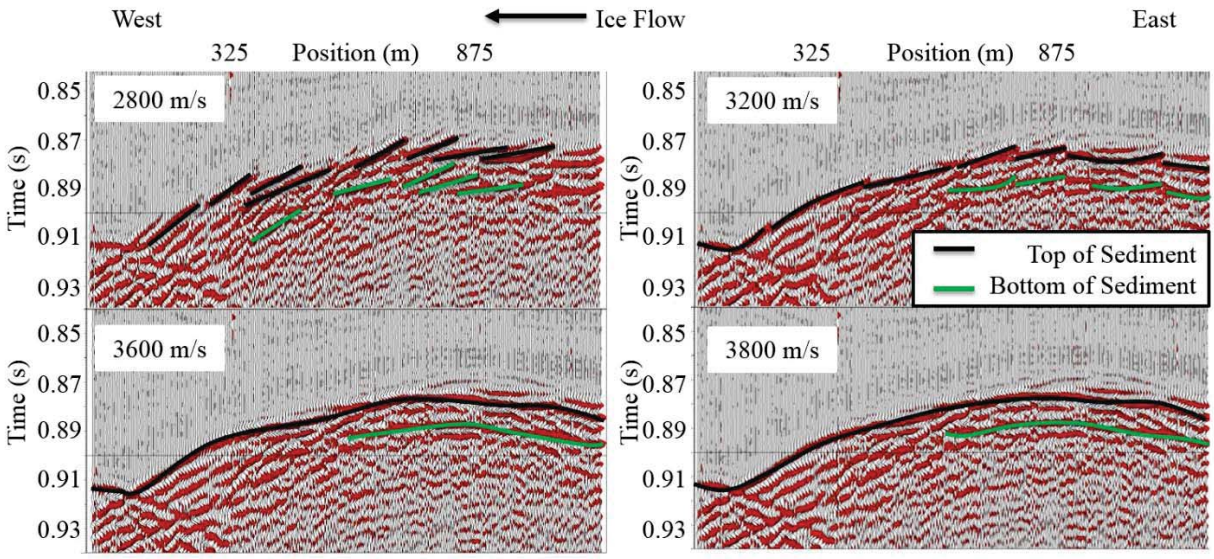

Figure 4.3: Migrated seismic panels using two-layer velocity models. Ice velocity is held constant to 3745 m/s. Sub-glacier sediment velocities are shown as inserts in each panel.

Bedrock is expected to be present below the sub-glacier sediments and to exhibit high velocity with small internal variability. As a result, diminished reflectivity is commonly observed within bedrock sections (Büker et al., 1998; Büker et al., 2000). Therefore, the transition between high amplitude continuous reflectors and low amplitude discontinuous reflectors was used to define a third velocity layer (Figure 4.4) thus dividing the sub-glacier geology into shallow sub-glacier sediments and bedrock. The velocity of the third deeper layer was estimated in an iterative fashion using velocities consistent with well-lithified materials from 4800 to 6800 m/s at 200 m/s intervals (Burger, 2006) and examining the continuity of deeper reflections, while using constant velocities for the ice and shallow sub-glacier layers. The third layer velocity that yielded the most coherent deeper section image was 5800 m/s, although weak and discontinuous deeper events made such determination challenging. Figure 4.5 shows the entire processed seismic profile using the three-layer velocity model with the interpretation of sub-glacier geology (refer to the interpretation section for additional information). Given the low fold of the data and the two dimensional nature of the acquisition it was not possible to completely focus the energy in the deeper portions of the profile.

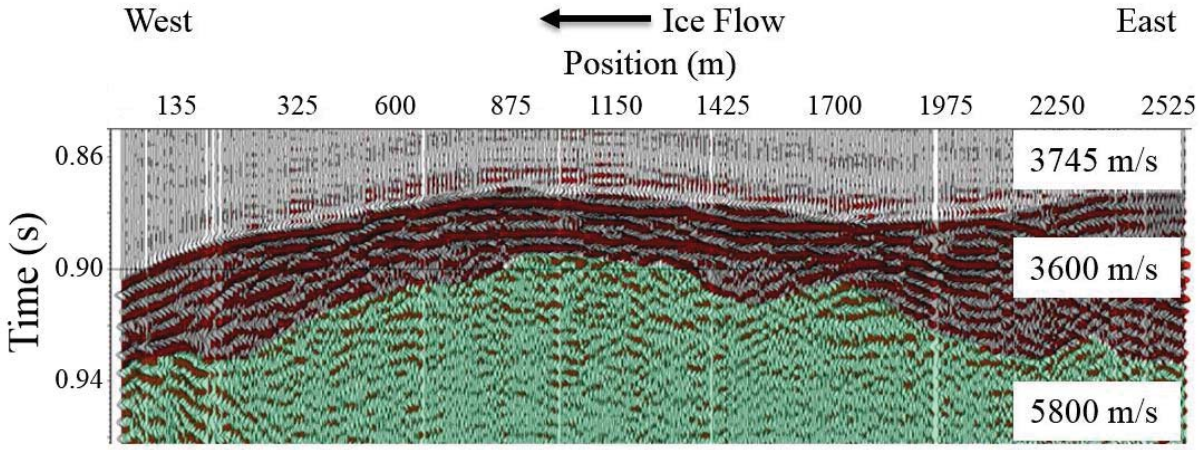

Figure 4.4: Section of the processed seismic line with amplitude data shown as wiggle traces and the three-layer velocity model as color overlay. Layer velocities are marked on the section.

4.4 INTERPRETATION

The seismic profile is located 100 km from the nearest outcrops along Greenland's west coast and no near-by ice cores are available (Figure 4.1). Therefore, it is not possible to establish a direct correlation between the seismic facies observed along the 2D line and sub-glacial depositional environments. However, information about subsurface geology can be obtained by comparing the geometry and distribution of seismic reflectors (referred to as seismic facies) to known geomorphological and sedimentary structures expected in glacial till and associated deposits. Furthermore, comparisons can be made with seismic facies observed at analogous depositional environments.

The ice/bed interface was imaged along the entire line (Figure 4.5) and marks the base of velocity layer one (the ice column) and the top of velocity layer two (the sub-glacier sediments). The top of the third velocity layer (the bedrock) was interpreted at the transition from high amplitude continuous reflections of layer two to low reflectivity discontinuous events below (Figure 4.5). The seismic character along with the high processing velocity of that interval (5800 m/s), leads to the interpretation of velocity layer three as the bedrock for the area of study (Figure 4.4).

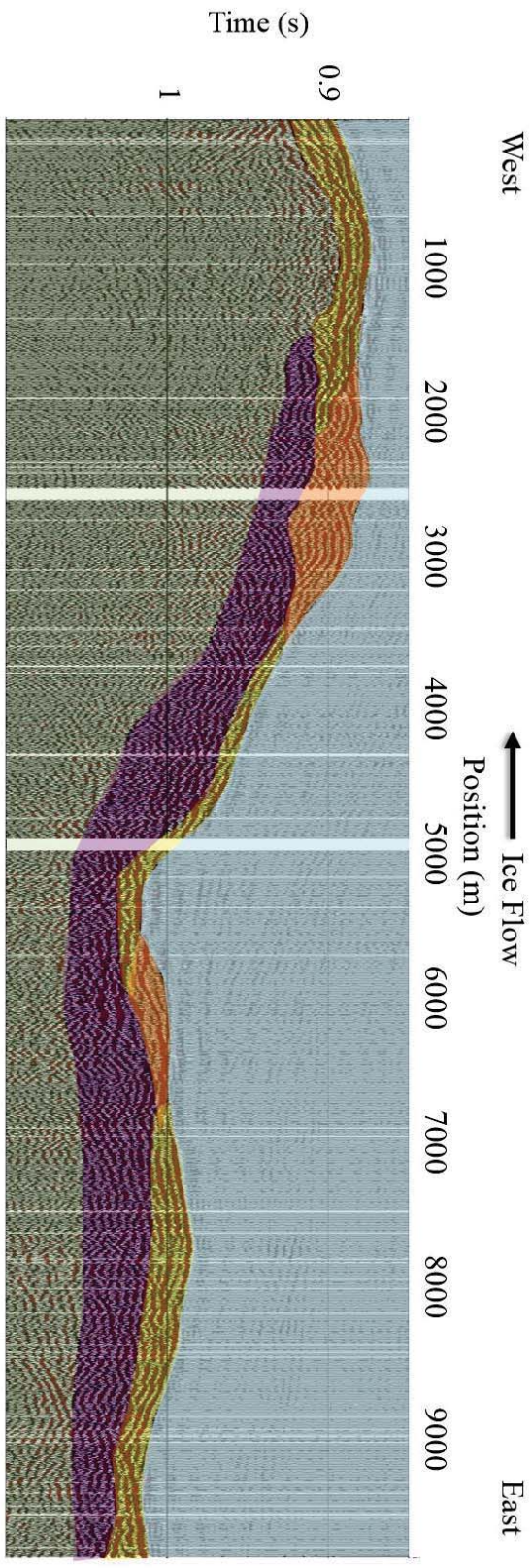

Figure 4.5: Seismic Facies interpreted along seismic line (see table I).

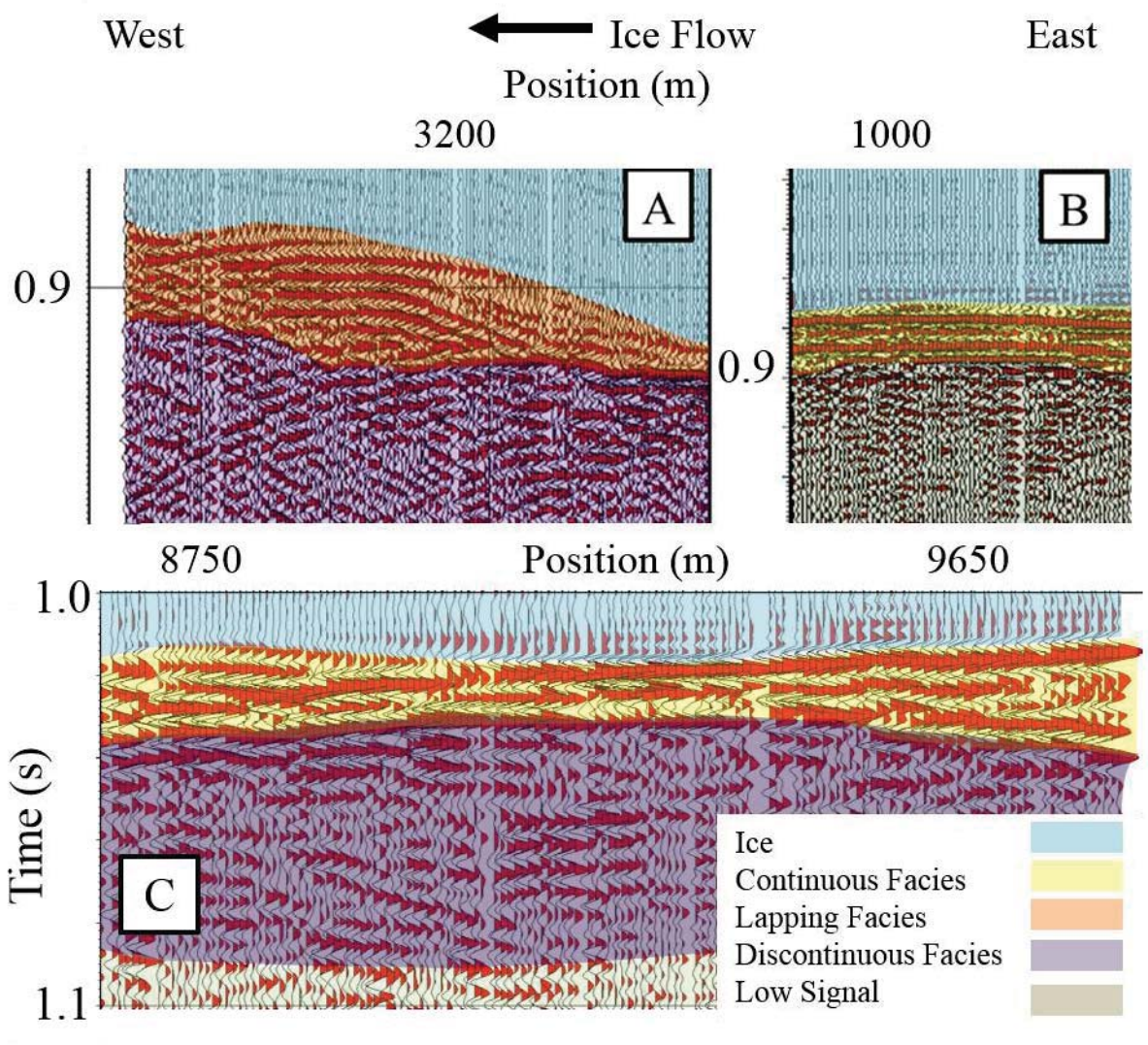

Figure 4.6: Sections of the seismic line showing examples of the sub-glacier sediment seismic facies: A) Re-worked sub-glacier sediments (discontinuous facies) overlaid by accreted sediments (lapping facies). B) Bedrock (low signal) overlaid by basal till (continuous facies) C) Bedrock (low signal) followed by re-worked sediment (discontinuous facies) overlaid by basal till (continuous facies). (see: table I for facies description).

Color	Facies	Interpretation	Order of Deposition
	Low Signal	Bedrock	1
	Discontinuous Reflectors	Reworked Till	2
	N/A	Ice	3
	Lapping Reflectors	Till Deposition	4
	Continuous Reflectors	Basal Till	4

Table (I): Description of seismic facies, deposition order and interpretation of seismic line of figures 4.6B based on facies interpretation of Büker et al., (2000) as well as Büker et al., (1998).

Sub-glacier sediments within velocity layer two range in thickness from 35 to 200 m and exhibit characteristic reflector geometries which were divided in to three distinct seismic facies: A) Discontinuous reflectors, B) Continuous reflectors and C) Lapping reflectors (Figures 4.5 and 4.6). The discontinuous reflector facies is observed over 80% of the profile and varies in thickness between 43 and 109 m, making it the most dominant facies of the dataset (Figure 4.5). This seismic facies is at the base of the sub-glacier sediments and it is associated with reworked till materials (Büker et al., 2000). The discontinuous reflector facies becomes prevalent in the sloping section of the profile while continuing toward the eastern portion of the line (Figure 4.5). The deep portion of the sloping section is disturbed by several seismic artifacts which make the interpretation of the slope difficult (Figure 4.5). In the eastern part of the line the discontinuous reflection facies increases in thickness (≈ 109 m) and is located beneath a continuous double reflector facies.

Approximately two thirds of the seismic line exhibits a continuous double reflector below the ice/bed interface and above the discontinuous facies described earlier (Figure 4.5). The continuous double reflector facies thickness is between 24 and 67 m (Figure 4.5). Seismic studies conducted over an analoguous depositional environment show a correlation between the continuous double reflector facies and a basal till layer based on a comparison between the seismic data and well log information (Büker et al., 2000). Investigations of till deposition and analysis of till depositional models (e.g. Evans et al., 2006) show that a stratified and inter-bedded sediment layer can be present at the base of a glacier. This depositional environment is possible when the basal till layer is continually replenished by eroded sediments from the up-flow direction (Evans et al., 2006). Based on the comparison of the continuous reflector facies

with similar seismic responses on data collected over paleo-till depositional environments (Büker et al., 2000) we interpret the continuous reflector facies as a basal till layer.

A lapping reflector facies is observed in areas of changing bed elevation (Figures 4.5, 4.6A) reaching a maximum thickness of 93 m. Given the area of study, the location of the lapping reflection facies, the geometry of the reflectors and the direction of ice flow (east to west), the most likely explanation for this facies is the accretion or deposition of sediments transported by the glacier. As seen in figure 4.6A, the lapping facies is characterized by continuous arcuate reflectors lapping over sub-glacier sediments.

As seen in Figure 4.5, both the lapping and continuous reflector facies are located above the bedrock and the discontinuous facies, and below the ice. Based on the principle of superposition, the reworked till material (discontinuous reflectors) must have been deposited before the basal till (continuous reflectors) and the accreted sediments (lapping reflectors). Therefore, the facies of continuous and lapping reflectors is interpreted as the zone of most recent sedimentary activity (e.g. deposition or deformation) and we will refer to it as the active sediment layer.

Close inspection of the ice bed interface shows evidence of reflection phase reversals at the topographic low region of the line (Figure 4.7, Position 4850). Seismic modeling was used to evaluate impedance contrasts and infer properties of geologic materials at the bed interface. A three-layer convolutional model was used where the middle layer varied in thickness (i.e. wedge model) and material properties. The source signal used for the model was a 190 Hz Ricker wavelet based on the frequency at the ice/bed interface reflection. Layer P-wave velocities and

densities are based on expected values for saturated sub-glacier sediments of high and low porosity, and water (Table II).

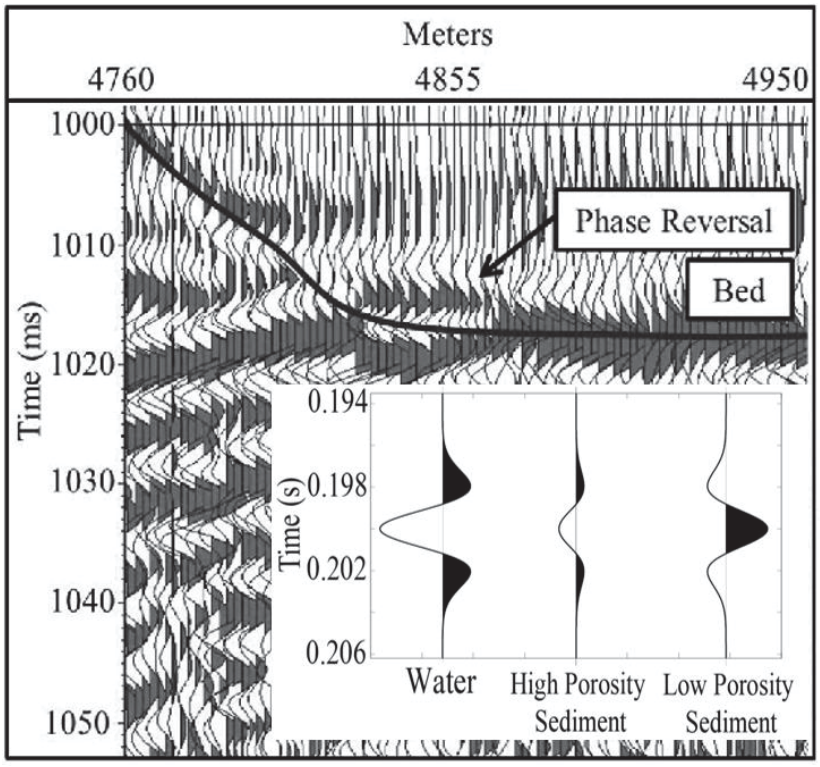

Figure 4.7: Phase reversal observed on seismic data at the ice bed interface (black line) attributed to a layer of water 2 m thick and 200 m wide. Insert: Waveforms modeled for layers of low and high porosity water saturated sediments and for a layer of water.

Material	Velocity (m/s)	Density (g/cc)
Ice	3745	0.97
Sediment	3600	2.2
Low Porosity Sediment	3200	2
High Porosity Sediment	1700	1.7
Water	1500	1

Table (II): Data used for wedge amplitude model. Material seismic properties (seismic velocity and density) were taken from Christensen (1989) with the exception of the ice velocity obtained based on seismic velocity analysis at the area of study.

The wedge models reveal that a positive reflection coefficient is expected at the ice/bed interface for low porosity water saturated tills, while a negative reflection coefficient is expected for high porosity water saturated tills and ponded water (Figure 4.7). The seismic profile shows positive amplitude reflections along the ice/bed interface, with the exception of the region where phase reversals occur (Figures 4.7). Therefore, most of the profile is interpreted to be underlain by low porosity water saturated tills. Furthermore, modeling shows that the negative reflection amplitudes resulting from the high porosity till are on average 50% less in magnitude than those observed for a water layer negative reflection or a low porosity till positive reflection. In order to assess the relative magnitude of the phase reversal reflections, amplitudes were extracted along the bed reflection and used to determine a mean low porosity till reflection magnitude baseline. The analysis shows that the amplitude magnitude extracted from traces exhibiting phase reversal is comparable to the amplitude response expected for a water-filled layer. For this reason the phase reversal is attributed to a sub-glacier river channel or ponded water. A study in this region using seismic attenuation showed evidence of pressure melting point temperatures at the ice bed interface (Peters et al., 2012). Therefore, the conditions at the ice/bed interface are favorable for the presence of liquid water in topographic low locations. Based on the quarter wavelength resolution criterion and using a velocity of propagation through water of 1,500 m/s and a signal frequency of 190 Hz, the water layer is estimated to be up to 2 m thick and 200 m wide.

4.5 SEDIMENT DEFORMATION

In this section, we provide an overview of the sediment deformation model used in this investigation and the assumptions involved in the estimation of the basal drag. Driving stress is

the force that makes ice flow in the direction of decreasing surface elevation and is given by the equation:

$$\tau_b = -\rho_{ice} g H \frac{\partial h}{\partial x} \quad (4.1)$$

were ρ_{ice} represents the density of ice (917 kg/m^3), g the earth gravitational constant (9.8 m/s^2), H the ice thickness, h the elevation of the ice surface and x is the coordinate in the flow direction (Van der Veen, 2013). The driving stress is opposed by resistive stresses that may originate at the glacier bed and at the lateral margins, or resistance may be associated with gradients in longitudinal stress. The area of study is located in the interior of the ice sheet, approximately 100 km from the mouth of the glacier (Figure 4.1), and the main resistance to flow is expected to originate at the glacier bed. This assumption allows basal drag to be estimated from the driving stress (equation 4.1). Adopting a linear viscous rheology for the sediment flow (Alley et al., 1987), the basal drag can also be estimated from the following equation (Van der Veen, 2013):

$$\tau_b = \underbrace{\frac{1}{2}\rho_{ice} g \frac{\partial H}{\partial x} H_t}_{A} - \underbrace{\rho_{till} g H_t \sin\theta}_{B} + \underbrace{\frac{\eta}{2}\frac{U_t}{H_t}}_{C} \quad (4.2)$$

were ρ_{till} is the till density, ρ_{ice} is the ice density, g the gravitational constant, H_t till thickness, θ is the slope of the bed, η is the viscosity of the till (kPa s) and U_t is the velocity of the till, and τ_b the drag at the ice/sediment interface. This shear stress is assumed to be constant throughout the comparatively thin sediment layer and resistance is transferred to the solid bedrock below.The terms on the right-hand side of equation (4.2) represent the effect of gradients in ice-overburden pressure (A), bed slope (B) and viscous deformation (C). With the

exception of till velocity and till viscosity, all variables on the right-hand side of equation 4.2 can be determined from the seismic data (ice thickness, till thickness and bed slope), whereas material density values can be taken from the literature (ρ_{till} = 2000 kg/m^3 and ρ_{ice} = 913 kg/m^3). The till thickness is the interval were the continuous and lapping facies are present (i.e. the active sediment layer) and a thickness profile is obtained using a sediment velocity of 3600 m/s (Figure 4.8A).

The till flow velocity is not known for the area of study, but making the assumption that all ice flow is the result of sediment deformation, no deformation occurs within the ice column and the measured surface speed (100 m/-a, Joughin et al., 2010) equals the till velocity at the top of the sediment layer. With this assumption, basal drag can be estimated from equation (4.2) for different values of viscosity. The viscosity which yields a basal drag similar to the driving stress would constitute the viscosity necessary for the deformable bed case at Jakobshavn Isbræ.

The only two available estimations of sub-glacier sediment viscosity were presented by Boulton and Hindmarsh (1987), obtained from direct measurements at the Breidamerkurjökull Glacier in Iceland ($6.5\ 10^{10}$ to $5.6\ 10^{11}$ Pa s). Using these viscosity values, equation (4.2) predicts basal drag values between -87 and 166 kPa and -87 and 155 kPa, respectively. These values fall outside the range of basal drag estimated from the driving stress (111 to 145 kPa; Figure 4.8B). In order to achieve a mean basal drag value of 135 kPa that corresponds to the average driving stress, a viscosity of $3.6\ 10^{12}$ Pa s must be used (Figure 4.8B).

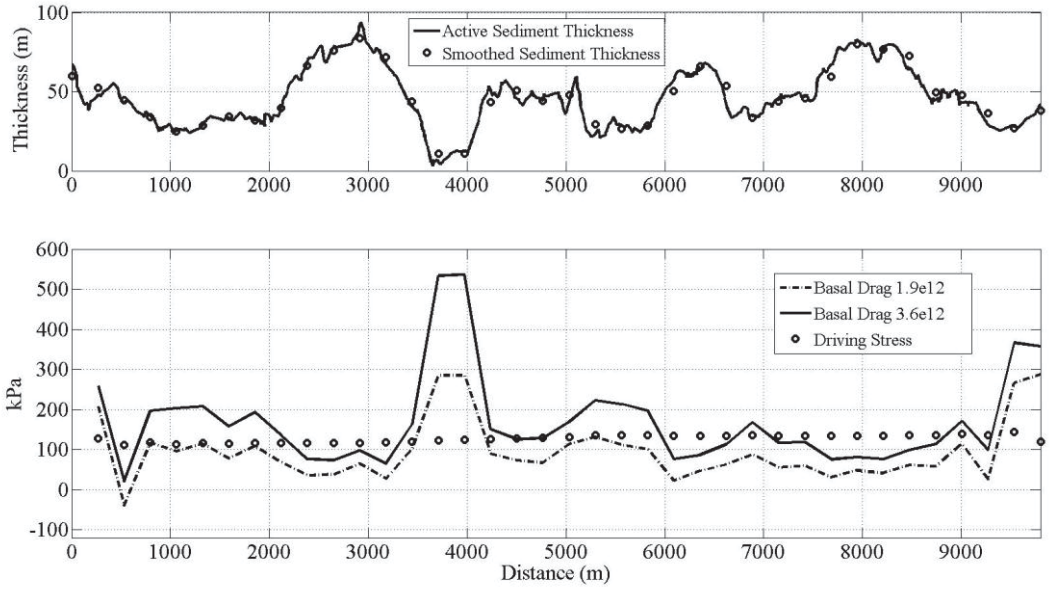

Figure 4.8: A) Active sediment layer thickness extracted from seismic line (Figure 4.5) and smoothed thickness used for basal drag modeling. B) Driving stress for area of study (equation 4.1: open circles) and basal drag (using equation 4.2) for two viscosities: 3.6 10^{12} and 1.9 e^{11} Pa s.

4.6 SEDIMENT DEFORMATION DISCUSSION

The combination of the study location and depositional environments interpreted from the seismic facies allows for the reconstruction of the depositional history in the area of study (see: Figure 4.5-4.6 and Table I). The interpretation of the basal till coupled to evidence of accreted sediments, points to the possibility of active sub-glacier sediment transport for the area of study. Eighty-percent of the reworked till is covered by either the basal till or accreted sediments. Following the law superposition, the reworked till layer may have been deposited above the bed rock before the deposition of the basal till layer and may pre-date the formation of the current ice sheet. Erosion and sediment transport resulted in the deposition of the basal till and accreted sediments above the reworked till layer. The lapping (accreted sediments) and continuous reflector (basal till) facies may represent the sediment actively transported today. As a result, a layer which includes the lapping and continuous reflector facies is interpreted and the thickness of this layer is estimated based on a seismic velocity of 3600 m/s (Figure 4.8A). The analysis of the extracted horizons shows that this layer varies in thickness between 4 and 93 m. The decrease in thickness of the double reflector and down-lapping facies in the slope region (Figures 4.5 and 4.8A, position 3600 to 4000 m) may be the consequence of an intensification of basal drag caused by an increase in bed elevation resulting in a zone of erosion. However, the exact flow state of the till layer (thickening, thinning or steady state) or conclusive evidence of active sediment transport cannot be obtained from the data available.

Adopting a linear viscous model for deformation of the active sediment layer, basal drag was estimated and compared to the driving stress. The viscosity necessary for the basal drag to match the mean driving stress is 3.6 10^{12} Pa s (Figure 4.8B). However, using this viscosity along the

entire line results in an unrealistically large peak in basal drag (533 kPa) in the area of decreased layer thickness near position 4000 m (Figure 4.8). This spike is due to the viscosity term C in equation (4.2) and can be eliminated by using a smaller viscosity.

Water saturation may significantly influence the deformation of sediments due to its effects on viscosity (e.g. Boulton and Jones, 1979; Clarke et al., 1984). In the case of the Breidamerkurjökull Glacier, analysis of sediment deformation combined with active pumping tests conducted at the bottom of the glacier showed a direct correlation between a decrease in sediment viscosity (more deformable) and an increase in water pressure (Boulton and Hindmarsh, 1987). The analysis of the seismic data in this investigation shows evidence for water at the bed of Jakobshavn Isbræ (Figure 4.7). Therefore, the sediment in the area of study could be saturated which is not compatible with high viscosity values. As a result, a second viscosity, 1.9 10^{12} Pa s, was used to obtain balance between the driving stress and the basal drag for the slope region (3500-4300 m: Figure 4.5) of the area of study and account for highly saturated sediments transported from the pond region (5200 m: Figure 4.7). Thus, a dual viscosity model is necessary for the deformable bed assumption to be compatible with glaciological observations (Figure 4.8B).

4.7 CHAPTER III: CONCLUSIONS

A 9.8 km seismic line was re-processed using an iterative seismic velocity processing approached in order to optimize the imaging of sub-glacier materials. Close examination of the iterative velocity analysis yielded two layers of sub-glacier velocities which were interpreted as sub-glacier sediments (Velocity Layer 2: 3600 m/s,) and the bedrock (Velocity Layer 3: 5800

m/s). The sub-glacier sediments were divided into three seismic facies (continuous, lapping and discontinuous reflectors) which are thought to correspond to three depositional environments (basal till, accreted sediments, and re-worked till) allowing for an interpretation of the depositional history of the sub glacial sediments beneath the Jakobshavn catchment region for the area of study (Figure 4.5-4.6 and Table I). The lapping and continuous reflectors were interpreted as the youngest depositional facies and may act as a lubrication layer varying in thickness between 4 and 93 meters.

Close examination of the reflection amplitudes at the ice/bed interface show phase reversals at the topographic low region of the line (Figure 4.7). Simulations of the ice/bed interface amplitude response using velocities and densities expected for till sediments under varying levels of water saturation as well as water (Table II) show that the best explanation for the phase reversals is the presence of water ponding or a sub-glacier river channel. The water layer is estimated to be approximately 2 m thick and 200 m wide.

The analysis of a deforming sediment layer showed that a dual viscosity model of 1.9 10^{12} and 3.6 10^{12} Pa s is needed to balance the basal drag and the driving stress at Jakobshavn Isbræ. Given that the maximum viscosity estimated at the Breidamerkurjokull Glacier (5.6 10^{11} Pa s) is within one order of magnitude to our estimated viscosities, we can conclude that the linear viscous model yields acceptable results in this study. The viscosity term is the dominant term in the basal drag equation 4.2 for deforming sediment, and the model is very sensitive to variations in till thickness. Given the presence of sub-glacier sediments along the entire seismic line, it is possible that sediments are common for the catchment region of Jakobshavn Isbræ. Therefore, further testing needs to be conducted to determine if a deforming bed model is appropriate for Jakobshavn Isbræ.

5.0 SUMMARY AND CONCLUSIONS

Several important conclusions resulted from this investigation. In the case of the NEEM radar experiment it was possible to detect the presence of three distinct COF patterns (isotropic, disc and single maxima) and the transition between each fabric using single frequency ground based radar measurements. Furthermore, it was possible to detect the presence of COF using single frequency grid radar measurements at multiple depths along the ice column by using the variation in backscatter power between orthogonal lines. It was not possible to detect the presence of COF using airborne radar measurements. However, future work using straight flight paths might yield variation in backscatter power resultant from COF as a function of flight path orientation.

The seismic experiment at NEEM successfully detected the presence of COF, confirming the feasibility of the Blankenship and Bentley method. However, it was not possible to fit the mean slowness results to one single model of I due to the variation of seismic velocity traveling through different parts of the disc ice fabric as the angle of incidence increases. The use of multi-azimuthal data should substantially increase the robustness of the analysis, thus allowing the comparison between the mean ice crystal orientation based on direct ice crystal measurements and the mean ice crystal orientation based on the seismic anisotropy analysis.

In the case of the seismic experiment preformed at NEEM, no reflectors were observed in the areas of transition between COF. This is attributed to the thickness of the transition zone (> 100 m). An important observation is that while the presence of englacial reflectivity provides evidence of COF development, the absence of reflectivity does not exclude the presence of COF layers.

Finally, the experiment in Jakobshavn Isbræ showed the feasibility of iterative velocity analysis to determine the sub-glacier sediment velocity by exploiting the continuity of the bed. The interpretation of the processed seismic line yielded three distinct seismic facies that point to the possibility of active sediment transport for the area of study. The interpreted zone of active sediment ranges in thickness between 5-80 m. The analysis of the bed showed phase reversals at the ice/bed which were attributed to the presence of water. Using the information extracted from the seismic experiment (i.e. bed geometry, ice and sub-glacier sediment thicknesses) and satellite based ice flow velocity estimations for the area of study, we provided an estimation of the sub-glacier sediment viscosity for the area of study, by means of a linear viscosity model based on the assumption of ice flow controlled by a deforming bed. The viscosity necessary for the basal drag to match the mean of the driving stress is 3.6 10^{12} Pa s. Given the presence of water at the bed and the high viscosities necessary for the model, the deformable bed assumption may not be appropriate for the area of study.

6.0 REFERENCES

Alley, R.B., Blankenship, D.D., Bentley, C.R., Rooney, S.T., (1986). Deformation of till beneath Ice Stream B, West Antarctica. Nature 322, 57–59.

Alley, R.B., Blankenship, D.D., Rooney, S.T., Bentley, C.R., (1987). Continuous till deformation beneath ice sheets. Publication of the International Association of Hydrological Sciences 170, 81–90.

Bindschadler, R., et al. (2013), Ice-sheet model sensitivities to environmental forcing and their use in projecting future sea level (The SeaRISE Project), J. Glaciol., 50, 195–224, doi:10.3189/2013JoG12J125.

Bentley, C. R. (1971), Seismic evidence for moraine within the basal Antarctic ice sheet, in Antarctic Snow and Ice Studies II, Antarct. Res. Ser., vol. 16, edited by A. P. Crary, pp. 89–129, AGU, Washington, D. C.

Bentley, C. R. (1986), P-Wave Anisotropy in the high polar ice of east Antarctica, Master thesis, Univ. of Wis.-Madison, Madison.

Bennett, H. F., 1968, An investigation into velocity anisotropy through measurements of ultrasonic wave velocities in snow and ice cores from Greenland and Antarctica. Ph.D. Thesis, University of Wisconsin-Madison.

Blankenship, D.D., 1982, P-wave anisotropy in the high polar ice of East Antarctica. M.S. thesis, University of Wisconsin-Madison.

Blankenship, D. D., C. R. Bentley, S. T. Rooney, and R. B. Alley (1987), Till beneath ice stream B 1: Properties derived from seismic travel times, J. Geophys. Res., 92(B9), 8903– 8911.

Block, A. E., and Bell, R. E., (2011) Geophysical evidence for soft bed sliding at Jakobshavn Isbrae, West Greenland. The Cryosphere Discuss., 5, 339–366, 2011.

Boulton, G. S., and R. C. A. Hindmarsh (1987). Sediment deformation beneath glaciers: Rheology and geological consequences. *Journ. Geoph. Res.* 92(B), 9059–9082.

Budd, W. F., D. Jenssen, and I. N. Smith (1984), A three-dimensional time-dependent model of the West Antarctic ice sheet, Ann. Glaciol., Pag 29-36.

Bogorodsky, V., C. Bentley and P. Gudmandsen (1985), Radio Glaciology, D. Reidel Publishing Co., ISBN.

Christensen, N. I. (1989), Seismic velocities, in CRC Practical Handbook of Physical Properties of Rocks and Minerals, edited by R. S. Carmichael, pp. 429– 546, CRC Press, Boca Raton, Fla.

Clarke, T. S., and K., Echelmeyer, (1996) SeislIlic-reflection evidence for a deep sub-glacial trough beneath Jakobshavns Isbrre, West Greenland. Journal of Glaciology, Vol. 43, No. 141.

Clough, J.W. (1977). Radio-echo sounding: reflections from internal layers in ice sheets. *J. Glaciol.*, 18 (78), 3-14.

Csatho, B., A. Schenk, C.J. Van der Veen, G. Babonis, K. Duncan, S. Rezvanbehbahanic, M. R. Van den Broeke, S. B. Simonsen, S. Nagarajan, and J. H. Van Angelen, 2014, Laser altimetry reveals complex pattern of Greenland Ice Sheet dynamics. PNAS, Vol. 111 No. 52

Csatho, B., T. Schenk, C.J. Van der Veen, and W. B. Krabill (2008), Intermittent thinning of Jakobshavn Isbræ, West Greenland, since the Little Ice Age, *J. Glaciol., 54(184), 131-144.*

Dahl-Jensen, D., M. R. Albert, A. Aldahan, N. Azuma, D. Balslev Clausen, M. Baumgartner, M. Baumgartner, A.-M. Berggren, M. Bigler, T. Binder, T. Blunier, T. Blunier, J. C. Bourgeois, E. J. Brook, S. L. Buchardt, C. Buizert, E. Capron, J. Chappellaz, J. Chung, H. B. Clausen, I. Cvijanovic, S. M. Davies, P. Ditlevsen, O. Eicher, H. Fischer, D. A. Fisher, L. G. Fleet, G. Gfeller, V. Gkinis, S. Gogineni, K. Goto-Azuma, A. Grinsted, H. Gudlaugsdottir, M. Guillevic, S. B. Hansen, M. Hansson, M. Hirabayashi, S. Hong, S. D. Hur, Huybrechts, P. C. S. Hvidberg, Y. Iizuka, T. Jenk, S. J. Johnsen, T. R. Jones, J. Jouzel, N. B. Karlsson, K. Kawamura, K. Keegan, E. Kettner, S. Kipfstuhl, H. A. Kjær, M. Koutnik, T. Kuramoto, P. Köhler, T. Laepple, A. Landais, P. L. Langen, L. B. Larsen, D. Leuenberger, M. Leuenberger, C. Leuschen, J. Li, V. L., Martinerie, P., Maselli, O. J., Masson-Delmotte, V., McConnell, J. R., Miller, H., Mini, O., Miyamoto, A., Montagnat-Rentier, M., Mulvaney, R., Muscheler, R., Orsi, A. J., Paden, J., Panton, C., Pattyn, F., Petit, J.-R., Pol, K., Popp, T., Possnert, G., Prié, F., Prokopiou, M., Quiquet, A., Rasmussen, S. O., Raynaud, D., Ren, J., Reutenauer, C., Ritz, C., Röckmann, T., Rosen, J. L., Rubino, M., Rybak, O., Samyn, D., Sapart, C. J., Schilt, A., Schmidt, A. M. Z., Schwander, J., Schüpbach, S., Seierstad, I., Severinghaus, J. P., Sheldon, S., Simonsen, S. B., Sjolte, J., Solgaard, A. M., Sowers, T., Sperlich, P., Steen-Larsen, H. C., Steffen, K., Steffensen, J. P., Steinhage, D., Stocker, T. F., Stowasser, C., Sturevik, A. S., Sturges, W. T., Sveinbjörnsdottir, A., Svensson, A., Tison, J.-L., Uetake, J., Vallelonga, P., van de Wal, R. S. W., van der Wel, G., Vaughn, B. H., Vinther, B., Waddington, E., Wegner, A., Weikusat, I., White, J. W. C., Wilhelms, F., Winstrup, M., Witrant, E., Wolff, E.W., Xiao, C., and J. Zheng, 2013, Eemian interglacial reconstructed from a Greenland folded ice core. Nature, 493, 489–494,

Dahl-Jensen, D., 1985, Determination of the flow properties at DYE 3, south Greenland, by borehole-tilting measurements and perturbation modeling. Journ. Glaciol. 31: 92-98

Ferrick, M., and K. Claffey, 1992, Vector Analysis of Ice Fabric Data. U.S. Army Corps of Engineers Cold Regions Research and Engineering Laboratories. CRREL Repost 92-1.

Fujita, S., and S. Mae, (1994), Causes and nature of ice-sheet radio-echo internal reflections estimated from the dielectric properties of ice. Annals of Glaciology, 20, 80-86.

Fujita, S., S. Mae and T. Matsuoka.(1993). Dielectric anisotropy in ice Ih at 9.7GHz. *Ann. Glaciol.*, **17**, 276-280.

Hargreaves, N. D. (1977), Polarization of radio signals in radio echo sounding of ice sheets, J. Phys. D Appl. Phys., 10(9), 1285–1304, doi:10.1088/0022-3727/10/9/012.

Harrison, C.H., (1973) Radio echo sounding of horizontal layers in ice. *J. Glaciol.*, 12 (66), 383-397.

Horgan, H. J., S. Anandakrishnan, R. B. Alley, L. E. Peters, G. P. Tsoflias, D. E. Voigt, and J. P. Winberry (2008), Complex fabric development revealed by englacial seismic reflectivity: Jakobshavn Isbræ, Greenland, *Geophysical Research Letters. Vol. 35, L105.*

Hofstede, C., O. Eisen, A. Diez, D. Jansen, Y. Kristoffersen, A. Lambrecht, and C. Mayer, 2013, Investigating englacial reflections with vibro- and explosive-seismic surveys at Halvfarryggen ice dome, Antarctica , Annals of Glaciology, 54 (64), pp. 189-200.

Hooke, R. L., (1981), Flow law for polycrystalline ice in glaciers: Comparison of theoretical predictions, laboratory data, and field measurements, Rev. Geophys., 19(4), 664–672.

Horgan, H. J., S. Anandakrishnan, R. B. Alley, P. G. Burkett and L. E. Peters, 2011, Englacial seismic reflectivity: imaging crystal-orientation fabric in West Antarctica. Journal of Glaciology, Vol. 57, No. 204.

Howat, I.M., I. Joughin, M. Fahnestock, B.E. Smith and T. Scambos. (2008), Synchronous retreat and acceleration of southeast Greenland outlet glaciers 2000–2006: ice dynamics and coupling to climate. *J. Glaciol.,* **54**(187), 646–660.

IPCC, 2014: Climate Change 2014: Mitigation of Climate Change. Contribution of Working Group III to the Fifth Assessment Report of the Intergovernmental Panel on Climate Change. Cambridge University Press, Cambridge, United Kingdom and New York, NY, USA.

Iken, A., K. Echelmeyer and W. D. Harrison. (1989) A light-weight hot water drill for large depth: experiences with drilling on Jakobshavns glacier, Greenland. In Rado, C. and D. Beaudoing, eds. Ice core drilling. Proceedings of the Third international Workshop on Ice *Drilling Technology* Grenoble- France. 10-14 October 1988. Grenoble, Laboratoire de Glaciologie et Gcophysique de I'Environnement , 123- 136.

Joughin, I., B. E. Smith, D. E. Shean, and D. Floricioiu (2014). Brief Communication: Further summer speedup of Jakobshavn Isbræ. The Cryosphere, 8, 209–214.

Joughin, I., B. Smith, I. Howat, and T. Scambos (2010), MEaSUREs Greenland Ice Sheet Velocity Map from InSAR Data, Boulder, Colorado, USA: National Snow and Ice Data Center. Digital media.

Kohnen, H., 1974, The temperature dependence of seismic waves in ice, J. Glaciol., 13, 144–147.

Luthcke, S. B., H. J. Zwally, W. Abdalati, D. D. Rowlands, R. D. Ray, R. S. Nerem, F. G. Lemoine, J. J. McCarthy and D. S. Chinn, (2006), Recent Greenland Ice Mass Loss by Drainage System from Satellite Gravity Observations. Science, Vol. 314, Pag: 1286-1289.

Matsuoka, K., D. Power, S. Fujita, and C. F. Raymond, (2012), Rapid development of anisotropic ice-crystal-alignment fabrics inferred from englacial radar polarimetry, central West Antarctica. Journal of Geophysical Research, Vol. 117, F03029, doi:10.1029/2012JF002440.

Matsuoka, K., T. Furukawa, S. Fujita, H. Maeno, S. Uratsuka, R. Naruse, and O. Watanabe., (2003) Crystal orientation fabrics within the Antarctic ice sheet revealed by a multi-polarization plane and dual-frequency radar survey. Journal of Geophysical Research, Vol. 108, No. B10, 2499, doi:10.1029/2003JB002425, 2003

Matsuoka, T., S. Fujita, S. Morishima, and S. Mae, (1997),Precise measurement of dielectric anisotropy in ice Ih at 39 GHz, J. Appl. Phys., 81(5), 2344–2348.

Matsuoka, K., S. Fujita, T. Matsuoka,T. Ishida, T. Hondoh and S. Mae., (1996) Measurement of the complex permittivity of acid-doped ice from 1 kHz to 30MHzönewdata set for developing ice radar and dielectric analysis of ice cores. *Proc. NIPR Symp. PolarMeteorol. Glaciol.* 10, 25-35.

Millar, D. H. M., (1982), Acidity Levels in Ice Sheets from Radio Echo-Sounding. Annals of Glaciology (3).

Murray, T., (1997) Assessing the paradigm shift: deformable glacier beds. Quaternary Science Reviews 16, 995–1016.

Moon, T. and I. Joughin, (2008), Changes in ice front position on Greenland's outlet glaciers from 1992 to 2007. *J. Geophys. Res.*, **113**(F2), F02022. (10.1029/2007JF000927.)

Moore, J.C. and Fujita, S. (1993). Dielectric properties of ice containing acid and salt impurity at microwave and low frequencies. *Journal of Geophysical Research 98: doi: 10.1029/93JB00710.*

Moore, J.C., (1988) Dielectric variability of a 130m Antarctic ice core: implications for radar sounding. *Ann. Glaciol.*, 11, 95-99.

Moore, J. C. and S. Fujita, (1993) Dielectric properties of ice containing acid and salt impurity at microwave and low frequencies. *J. Geophys. Res.*, 98 (B6), 9769^9780.

Montagnat, M., N. Azuma, D. Dahl-Jensen, J. Eichler, S. Fujita, F. Gillet-Chaulet, S. Kipfstuhl, D. Samyn, A. Svensson, and I. Weikusat, 2014, Fabric along the NEEM ice core, Greenland, and its comparison with GRIP and NGRIP ice cores , The Cryosphere, 8 (4), pp. 1129-1138.

Nye J. F., (1957), Physical properties of crystals. Oxford University Press, USA.

Payne, A. J., (1997), Self-organization in the thermomechanical flow of ice Sheets. Journal of Geophysical Research, Vol. 102, NO. B6, Pag, 12,219-12,233.

Peters, G. P., S. Anandakrishnan, R. B. Alley, and D. E. Voigt, 2012, Seismic attenuation in glacial ice: A proxy for englacial temperature, J. Geophysical Research, Vol. 117.

Peters, L. E., S., Anandakrishnan, Alley, R. B., and A. M., Smith, (2007), Extensive storage of basal meltwater in the onset region of a major West Antarctic ice stream. *Geology*, March, *2007, v. 35, p. 251-254.*

Rasmussen, S. O., P. M. Abbott, T. Blunier, A. J. Bourne, E. Brook, S. L. Buchardt, C. Buizert, J. Chappellaz, H. B. Clausen, E. Cook, D. Dahl-Jensen, S. M. Davies, M. Guillevic, S. Kipfstuhl, T. Laepple, I. K. Seierstad, J. P. Severinghaus, J. P. Steffensen, C. Stowasser, A. Svensson, P. Vallelonga, B. M. Vinther, F. Wilhelms, and M. Winstrup, 2013, A first chronology for the North Greenland Eemian Ice Drilling (NEEM) ice core. Clim. Past, 9, 2713–2730.

Rignot, E. and P. Kanagaratnam (2006), Changes in the velocity structure of the Greenland Ice Sheet. *Science, 311(5673), 986–990.*

Rignot, E., J. E. Box, E. Burgess, and E. Hanna (2008), Mass balance of the Greenland ice sheet from 1958 to 2007, Geophys. Res. Lett., 35, L20502, doi:10.1029/2008GL035417.

Robin, G. de Q., S. Evans, and J. T. Bailey, (1969), Interpretation of radio echo sounding in polar ice sheets, Philos. Trans. R. Soc. London, Ser. A, 265(166), Pag. 437-505.

Röthlisberger, H., 1972, Seismic exploration in cold regions. Technical report, Cold Reg. Res. and Eng. Lab, Hanover, N. H.

Paren, J.G. and G. de Q. Robin. (1975) Internal reflections in polar ice sheets. *J. Glaciol.*, 14 (71), 251^259.

Payne, A. J., (1995) Limit cycles in the basal thermal regime of ice sheets, J. Geophys. Res., 100(B3), 4249–4263.

Seddik, H., R. Greve, and S. Sugiyama, (2009), Numerical Simulation of the Evolution of Glacial Valley Cross Sections. arXiv:0901.1177v1 Physics.geo-ph.

Sheriff E. R., (2006), Encyclopedic Dictionary of Applied Geophysics, 4nd ed., Tulsa OK, Press, Society of Exploration Geophysics.

Smith, A. M., (2007), Subglacial Bed Properties from Normal-Incidence Seismic Reflection Data. JEEG, Volume 12, Issue 1, pp. 3–13

Smith, A. M., (1997), Variations in basal conditions on Rutford Ice Streatn.,West Antarctica. Journal of Glaciology, Vat. 43 No. 144.

Solomon, S. and 29 others. 2007. Technical summary. In Solomon, S. and 7 others, eds. Climate change 2007: the physical science basis. Contribution of Working Group I to the Fourth Assessment Report of the Intergovernmental Panel on Climate Change. Cambridge, etc., Cambridge University Press, 21–87.

Thomsen, L., (1986), Weak elastic anisotropy. Geophysics. Vol. 51. Pag. 1954-1966.

Tsvankin, I., (2005), Seismic signatures and analysis of reflection data in anisotropic media, Vol 29 ., 7-13 pp., Colorado School of Mines. Press, New York.

Velicogna, I., (2009), Increasing rates of ice mass loss from the Greenland and Antarctic ice sheets revealed by GRACE. Geophysical Research Letters, VOL. 36, L19503, doi:10.1029/2009GL040222.

Wang, W., J. Li, and H. J. Zwally, (2012), Dynamic Inland Propagation of Thinning due to Ice Loss at the Margins of the Greenland Ice Sheet. Jurnal of Glaciology, Vol. 58. No 210. Doi10.3189.

Van der Veen C. J. (2013), Fundamentals of Glacier Dynamics, Second Edition. Sound Parkway NW, Taylor & Francis Group, LLC.

Van der Veen, C.J., J.C. Plummer, and L.A. Stearns (2011), Controls on the recent speed-up of Jakobshavn Isbræ, West Greenland, *J. Glaciol., 57(204), 770-782.*

Van der Veen, C.J. and I.M. Whillans, 1994, Development of fabric in ice. Cold Regions Science and Technology, 22, 171-195.

Velez, A. J., (2012) Development of a Seismic Snow Streamer and Use of Multi-Offset Reflection for Determining Glacier Ice Properties. KU Thesis Submitted.

Widess, M.B., 1973, How thin is a thin bed, Geophysics,38, 1176-1180